# Simulations and observational tests of primordial magnetic fields from Cosmic Microwave Background constraints

F. Vazza[1,2,3]*, D. Paoletti[4,5], S. Banfi[1,3], F. Finelli[4,5], C. Gheller [3],
S. P. O'Sullivan[6], M. Brüggen[2]

[1] *Dipartimento di Fisica e Astronomia, Universitá di Bologna, Via Gobetti 92/3, 40121, Bologna, Italy*
[2] *Hamburger Sternwarte, Gojenbergsweg 112, 21029 Hamburg, Germany*
[3] *INAF, Istituto di Radio Astronomia, Via Gobetti 101, 40129 Bologna, Italy*
[4] *INAF, Osservatorio di astrofisica e scienza dello spazio, INAF, Via Gobetti 101, 40129 Bologna, Italy*
[5] *INFN, Sezione di Bologna, Via Irnerio 46, 40126 Bologna, Italy*
[6] *School of Physical Sciences and Centre for Astrophysics & Relativity, Dublin City University, Glasnevin, D09 W6Y4, Ireland*

**ABSTRACT**

We present the first cosmological simulations of primordial magnetic fields directly derived from the constraints from the Cosmic Microwave Background observations, based on the fields' gravitational effect on cosmological perturbations. We evolved different primordial magnetic field models from $z = 40$ to $z = 0$ with the *ENZO* code and compared their observable signatures (and relative differences) in galaxy clusters, filaments and voids. The differences in synchrotron radio powers and Faraday Rotation measure from galaxy clusters are generally too small to be detected, whereas differences present in filaments can only be investigated with the higher sensitivity afforded by the Square Kilometre Array. However, several statistical full-sky analyses, such as the cross-correlation between galaxies and diffuse synchrotron power, the Faraday Rotation structure functions from background radio galaxies, or the analysis of arrival direction of Ultra-High-Energy Cosmic Rays, may already be used to detect currently constrained fields.

**Key words:** galaxy: clusters, general – methods: numerical – intergalactic medium – large-scale structure of Universe

## 1 INTRODUCTION

Although we understand by and large how the inhomogeneities of the cosmic microwave background (CMB) at $z \sim 1100$ are related to the distribution of dark (DM) and baryonic matter, the origin of extragalactic magnetic fields is still a puzzle (e.g. Widrow 2002; Ryu et al. 2012; Widrow et al. 2012). It is generally believed that magnetic fields observed in galaxies (e.g. Beck et al. 2012; Pakmor et al. 2014; Rieder & Teyssier 2016, 2017, for recent work on the subject), or in the intracluster medium (e.g. Dolag et al. 1999; Brüggen et al. 2005; Ryu et al. 2008; Xu et al. 2009; Beresnyak & Miniati 2016a), are the result of amplification of weak seed fields (e.g. Donnert et al. 2018). However, it remains unclear whether such seed fields were already present at the epoch of the CMB, or whether they arose during the epoch of galaxy formation, following the release of magnetised winds and jets.

Several mechanisms to generate primordial seed fields have been suggested. These may either involve inflation or take place in the post-inflationary epoch, with the latter referred historically to as causal generation mechanisms. Causal magnetic fields can be possibly generated with large amplitudes, but suffer from small coherence lengths (with the size of the Hubble radius at the generation time being the maximum) and they thus require inverse cascade mechanisms to transfer energy to the largest scales. Among causal generation mechanisms, those associated with phase transitions as the electroweak or the QCD (e.g. Quashnock et al. 1989; Vachaspati 1991; Baym et al. 1996; Sigl et al. 1997; Hindmarsh & Everett 1998; Grasso & Riotto 1998; Ahonen & Enqvist 1998; Boyanovsky & de Vega 2005; Caprini et al. 2009; Tevzadze et al. 2012; Zhang et al. 2019; Ellis et al. 2019) are extremely important, but they require a first-order phase transition, which is currently disfavoured. Alternative causal mechanisms involve second-order perturbations via the Harrison mechanism and recombination, but these can generate only very weak final fields (Fidler et al. 2016; Fenu et al. 2011; Matarrese et al. 2005). A common characteristics of causal generation mechanisms is that the magnetic fields they produce have a scale-dependence, with a spectral index equal or greater than 2 (Durrer & Caprini 2003).

On the contrary, inflation can generate magnetic fields with different coherence lengths and scale dependencies (however, in this work we assume $-2.9$ as minimal index to avoid infrared divergences in the energy-momentum tensor of the fields). Magnetic fields can be generated during inflation by breaking the conformal invariance for the electromagnetic field, or by coupling it to other light fields (e.g. Turner & Widrow 1988; Ratra 1992; Giovannini & Shaposhnikov 2000; Törnkvist et al. 2001; Bamba & Yokoyama 2004; Ashoorioon & Mann 2005; Demozzi et al. 2009; Kanno et al. 2009; Caldwell et al. 2011; Jain et al. 2014; Fujita et al. 2015), and depending on the specific mechanism the resulting fields have different characteristics. Such primordial seed fields are found to produce either small ($\leqslant$ Mpc, e.g. Chernin 1967), or large (e.g. Zel'dovich 1970; Turner & Widrow 1988) coherence lengths, which may still persist today (e.g. Hutschenreuter et al. 2018), at least in the emptiest cosmic regions. Primordial magnetic fields can also possibly carry information on the generation of primordial helicity (e.g. Semikoz & Sokoloff 2005; Campanelli 2009; Kahniashvili et al. 2016). The subsequent amplification of these seed fields, plausible by the dynamo mechanism (see Donnert et al. 2018, for a recent review), further adds to the theoretical predictions of the primordial generation mechanisms.

Several different observations can be used to constrain primordial magnetic fields generated prior to Big Bang Nucleosynthesis. Magnetic fields with a primordial origin, modelled as a stochastic background, can be probed by the anisotropy pattern of the CMB. The analysis of the gravitational effect on the CMB anistropies angular power spectra in temperature and polarization with recent Planck (Akrami et al. 2018), BICEP/Keck Array (Ade et al. 2018), SPT (Keisler et al. 2015) data strongly constrains fields with amplitude values larger than a few co-moving $\sim$ nG on $\sim$ Mpc scales (Paoletti & Finelli 2019; Planck Collaboration et al. 2016; Zucca et al. 2017; Paoletti & Finelli 2013, 2011; Shaw & Lewis 2012). Corresponding bounds have been also derived for an homogeneous primordial magnetic field, whose main additional effect is the breaking of isotropy, that is constrained to very few nG already with COBE satellite data (Barrow et al. 1997). However, these bounds may be slightly relaxed in the presence of free-streaming neutrinos (Adamek et al. 2011; Jedamzik & Saveliev 2019). On the other hand, magnetic fields in cosmic voids are constrained to be larger than the lower limits deduced by the absence of an Inverse Compton Cascade from distant blazars (e.g. Dolag et al. 2009; Neronov & Vovk 2010; Dolag et al. 2011; Arlen et al. 2014; Caprini & Gabici 2015; Chen et al. 2015), of order $\sim 10^{-7}$ nG [1].

Any significant detection of magnetic fields beyond galaxies and galaxy clusters (or even any robust upper limit) would thus help to explore the origin of cosmic magnetism, because several theoretical works have shown that the radio signatures of drastically different magnetic field scenarios would leave very different imprints in Faraday Rotation and/or synchrotron emission from the magnetised cosmic web (Donnert et al. 2009; Vazza et al. 2015; Vazza et al. 2017). Due to the very weak radio signal expected outside of the overdensities typical of halos and cluster outskirts, different observational proxies have also been proposed, i.e. by studying the propagation of Ultra-High-Energy Cosmic Rays (e.g. Dolag et al. 2005; Hackstein et al. 2017), by using the non-detection of Inverse Compton halo emission from distant blazars. From this effect, lower limits of $\geqslant 10^{-16}$ G on $\sim$ Mpc scales have been derived (Dolag et al. 2009; Neronov & Vovk 2010; Dolag et al. 2011; Arlen

---

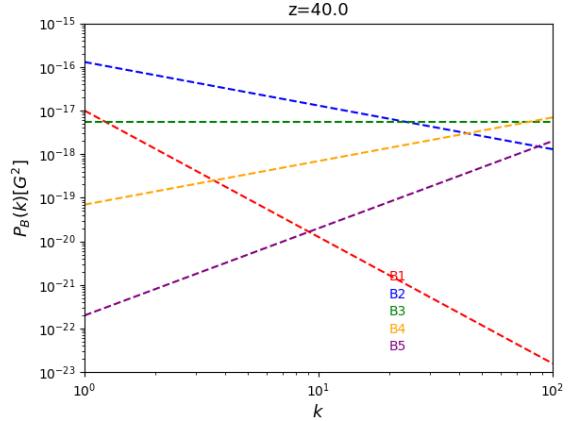[1] See however Broderick et al. (2012) for a possible different interpretation.



**Figure 1.** Input 3-dimensional power spectra ($z = 40$) of magnetic fields for our models.

et al. 2014; Caprini & Gabici 2015; Chen et al. 2015). In the near future, the Cherenkov Telescope Array (CTA) will have the potential to further limit large-scale magnetic fields through the same effect (Sol et al. 2013; Meyer et al. 2016).

Finally, the presence of significant large-scale magnetic fields has been suggested as a possible explanation for the puzzling lack of infrared absorption in the observed spectra of distant blazars (e.g. Tavecchio et al. 2012; Horns et al. 2012). Axion-like particles (ALPs) are promising candidate for DM (Raffelt & Stodolsky 1988; Csáki et al. 2003) and they can oscillate into high-energy photons (and back) in the presence of background magnetic fields, reducing the effective opacity of emitted γ-ray photons (Horns et al. 2012). With recent work we simulated the propagation of photons from redshift $z = 1$ and computed the expected conversion into ALPs, and we found that photons-ALPs oscillations are possible for lines of sight crossing structures with $\sim 1 - 10$ nG on scales of a few $\sim$ Mpc. (Montanino et al. 2017), and effect also likely to be testable using the upcoming CTA (Montanino et al. 2017).

In this work, we present for the first time cosmological simulations of primordial magnetic fields derived from the constraints from the CMB, based on the fields's gravitational effect on cosmological perturbations. By evolving different primordial magnetic field models from $z = 40$ to $z = 0$, we generated observable signatures across the cosmic web and used them to investigate whether further constraints can be put on primordial scenarios. This paper is structured as follows: after describing our simulations and numerical tools in Sec. 2, we present our results in Sec. 3. We provide physical and numerical caveats in Sec. 4 before we summarise and conclude our work in Sec. 5.

## 2 METHODS

### 2.1 Cosmological Simulations

We used the cosmological Eulerian code *ENZO* (Bryan et al. 2014) to resimulate a cosmic volume of $(100 \text{ Mpc})^3$ comoving, with the constant spatial resolution of $\Delta x = 195$ comoving kpc, using $512^3$ cells and Dark Matter particles. We investigate the evolution and topology of magnetic fields in the most rarefied cosmic regions, removed from the contamination from galaxy-related processes. In

**Table 1.** List of cosmological *ENZO* simulations produced for this work.

| Run ID | Volume [Mpc] | Resolution [kpc] | $\Omega_M$ | $\Omega_b$ | $\Omega_\Lambda$ | $\sigma_8$ | $h$ [100 km/s/Mpc] | $k_D$ [1/Mpc] | $B_{\mathrm{Mpc}}$ [nG] | $B_{\mathrm{eff}}$ [nG] | description |
|---|---|---|---|---|---|---|---|---|---|---|---|
| B0 | 100 | 195 | 0.308 | 0.0478 | 0.692 | 0.815 | 0.678 | - | 2.0 | 2.0 | homogeneous |
| B1 | 100 | 195 | 0.308 | 0.0478 | 0.692 | 0.815 | 0.678 | 84.7 | 2.0 | 2.53 | $\alpha = -2.9$ |
| B2 | 100 | 195 | 0.308 | 0.0478 | 0.692 | 0.815 | 0.678 | 25.8 | 1.87 | 47.63 | $\alpha = -1.0$ |
| B3 | 100 | 195 | 0.308 | 0.0478 | 0.692 | 0.815 | 0.678 | 37.6 | 0.35 | 70.1 | $\alpha = 0.0$ |
| B4 | 100 | 195 | 0.308 | 0.0478 | 0.692 | 0.815 | 0.678 | 56.6 | 0.042 | 95.21 | $\alpha = 1.0$ |
| B5 | 100 | 195 | 0.308 | 0.0478 | 0.692 | 0.815 | 0.678 | 87.9 | 0.003 | 119.21 | $\alpha = 2.0$ |
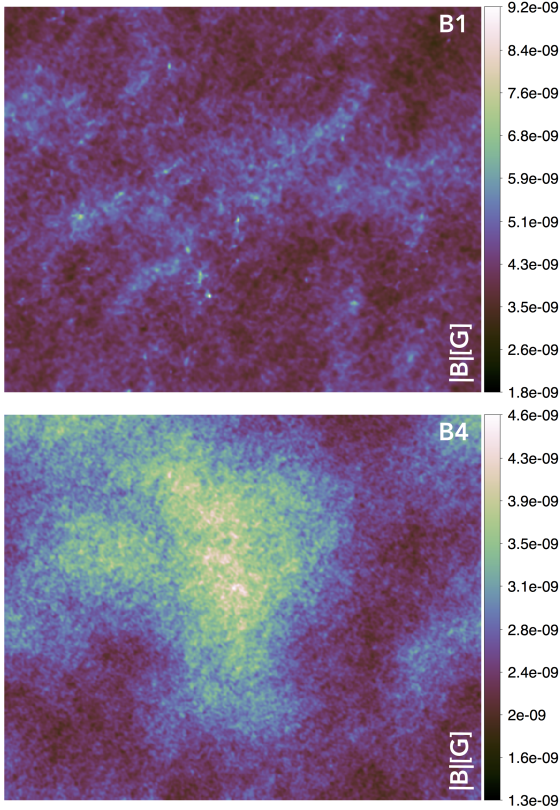


**Figure 2.** Projected (gas mass-weighted) physical magnetic field strength along the entire 100 Mpc line of sight for run B1 and B4 at the begin of our simulations ($z = 40$)

.

order to make up for the lack of resolution, we apply a scheme to include the dynamo amplification by unresolved turbulence, see e.g. Sec.2.1.2.

The adopted cosmology is a $\Lambda$CDM model with $\Omega_b = 0.0468$, $\Omega_m = 0.308$, $\Omega_\Lambda = 0.692$, $H_0 = 67.8$ km/s/Mpc, $\sigma_8 = 0.815$, and a spectral index for the initial matter power spectrum of $n = 1.0$ [2] and an initial redshift $z_{\mathrm{ini}} = 40$.

### 2.1.1 MHD method

The adopted scheme for magneto-hydrodynamics (MHD) is the conservative Dedner formulation (Dedner et al. 2002), which uses

hyperbolic divergence cleaning to keep the $\nabla \cdot \vec{B}$ as small as possible, in combination with the Piecewise Linear Method reconstruction (PLM) technique and with the Harten-Lax-Van Leer (HLL) approximate Riemann solver. The time integration is based the total variation diminishing (TVD) second-order Runge-Kutta (RK) scheme (Shu & Osher 1988).

The choice of using a constant spatial resolution, rather than an adaptive one, is related to the fact that all effects we are looking for in this project are related to underdense cosmic regions (e.g. voids) or mildly dense structures (e.g. matter sheets, filaments, cluster outskirts), and therefore the use of a fixed spatial resolution is helpful for our analysis. Tests on the dependence of some of our results on the spatial resolution are presented in the Appendix.

### 2.1.2 Subgrid Dynamo Model

Our simulations are non-radiative, i.e. only the effects of cosmological expansion, gravity and magneto-hydrodynamics are included. To make up for the lack of small-scale dynamo amplification in the turbulent interiors of halos, we applied a subgrid model for magnetic field amplification (Porter et al. 2015; Beresnyak & Miniati 2016a; Wittor et al. 2017b) within overdense regions ($\rho \geqslant 50\langle\rho\rangle$)(e.g. Vazza et al. 2017). At run time we measure the gas vorticity and use it to estimate the dissipation rate of solenoidal turbulence into magnetic field amplification. Our procedure is based on Federrath et al. (2014), and on their fitting formulas to predict the growth of magnetic energy from scales that our simulation cannot directly resolve.

The local velocity enstrophy, $(\nabla \times \vec{v})^2 \equiv \varepsilon_\omega$ is a convenient quantity to estimate the turbulent dissipation rate, because the turbulent kinetic energy flux is conserved along the cascade. Following previous work (Jones et al. 2011; Porter et al. 2015; Vazza et al. 2017; Wittor et al. 2017a), we assume that a small fraction, $\eta_t \approx 10^{-2}$, of such kinetic power gets channeled into the amplification of magnetic fields, $F_{\mathrm{turb}} \simeq \eta_t \rho \varepsilon_\omega^3 / L$, where $L$ is the stencil of cells to compute the vorticity. The fraction of turbulent kinetic power that gets converted into magnetic energy, $\varepsilon_{\mathrm{dyn}}$, sets the amplified magnetic energy as $E_{\mathrm{B,dyn}} = \varepsilon_{\mathrm{dyn}}(\mathscr{M})F_{\mathrm{turb}}\Delta t$. For a reasonable guess on $\eta_{\mathrm{dyn}}$, we rely on Federrath et al. (2014), who simulated small-scale dynamo in a variety of conditions for the forcing of turbulence. We can thus estimate the saturation level and the typical growth time of magnetic fields as a function of the local Mach number of the flow ($\mathscr{M}$), and set $\varepsilon_{\mathrm{dyn}}(\mathscr{M}) \approx (E_B/E_k)\Gamma\Delta t$, where $E_B/E_k$ is the estimated ratio between magnetic and kinetic energy at saturation and $\Gamma$ is the typical growth rate, taken from Federrath et al. (2014). In this approach, we need to specify the topology of the amplified magnetic field. For simplicity, the additional field is taken to be parallel to the gas vorticity in each cell, such that the newly generated field is solenodial by construction.
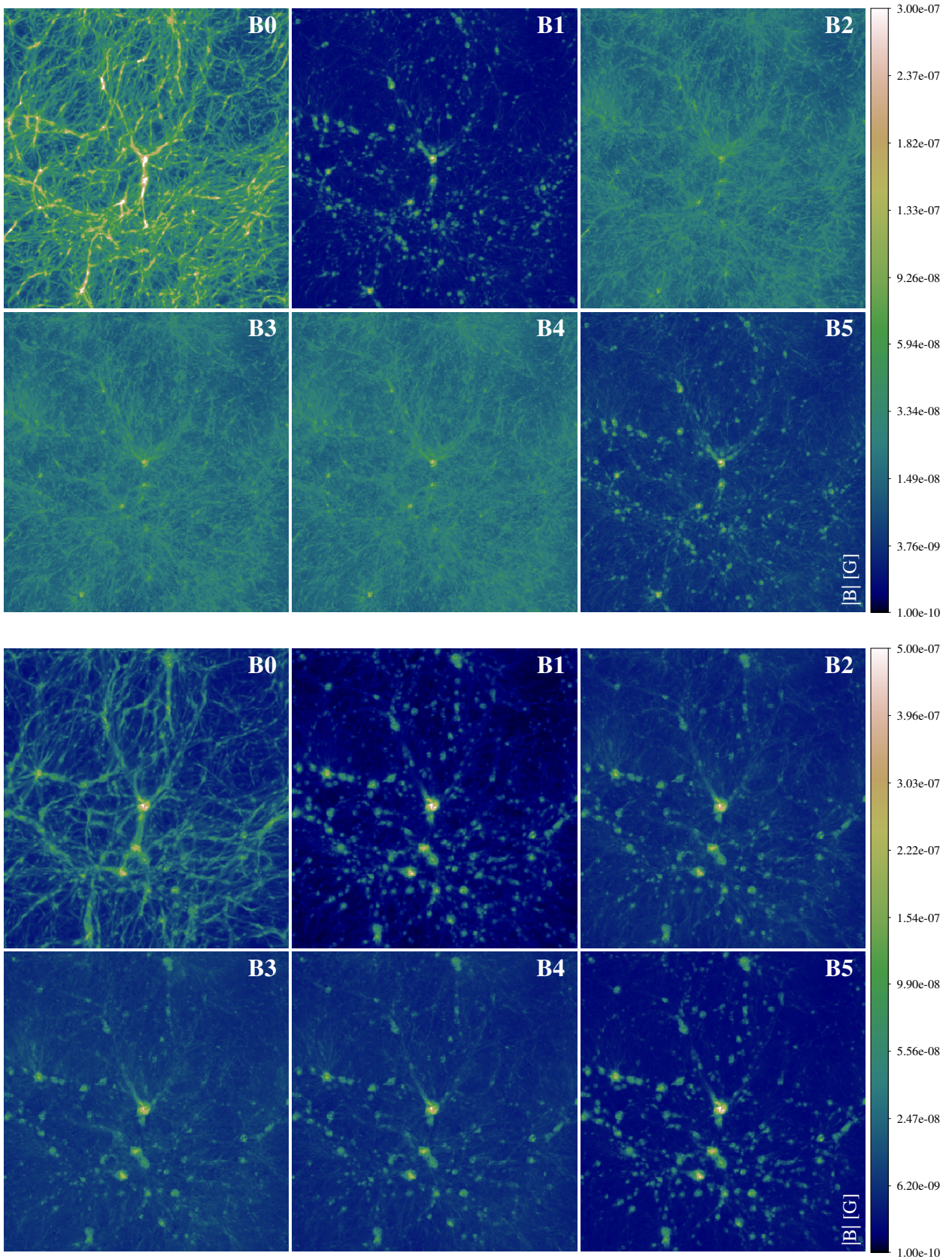
---

[2] Due to the little correlation of the scalar spectral index with the primordial magnetic field configuration we expect little dependence on the value of ns of the field final properties.

**Figure 3.** Projected (gas mass-weighted) proper magnetic field strength along the entire 100 Mpc line of sight, for all our models at $z = 1$ (top) and at $z = 0$ (bottom).

Energy and momentum are conserved assuming an isotropic dissipation of the small-scale velocity vectors. Admittedly, this procedure is simpler than more sophisticated subgrid models (Grete et al. 2016). However, we have shown that this simplistic method reproduced the results obtained by other methods (e.g. Ryu et al. 2008; Vazza et al. 2017; Hackstein et al. 2019). While the application of the sub-grid dynamo model adds realism to the magnetic field distribution in our volume, it has no impact on the intermediate and low-density regime in which we study the differences introduced by our CMB-based magnetic fields. As it solely relies on the gas velocity field, which is basically identical in all runs, the contribution from the sub-grid dynamo model within halos is exactly the same in all models.

### 2.1.3 *Primordial magnetic field models*

We modelled the primordial magnetic fields using a stochastic background, described by the two-point correlation function (Mack et al. 2002; Finelli et al. 2008):

$$\langle B_i^\star(\mathbf{k})B_j(\mathbf{k}')\rangle = \delta^{(3)}(\mathbf{k}-\mathbf{k}')P_{ij}(\hat{\mathbf{k}})P_B(k)(2\pi)^3, \qquad (1)$$

where $i$ and $j$ are spatial indices. $\delta^{(3)}(\mathbf{k}-\mathbf{k}')$ is the Dirac delta function, with unit vector $\hat{k}_i = k_i/k$ is a unit wavevector, $P_{ij}(\hat{\mathbf{k}}) = \delta_{ij} - \hat{k}_i\hat{k}_j$ is the operator for transverse plane projection, and $P_B(k)$ is the power spectrum of the magnetic field. The fields scale dependence can be described with a power law power spectrum: $P_B(k) = P_{B0}k^\alpha$ characterised by the amplitude of the fields and the spectral index. As a convention, we describe the amplitude by smoothing the fields on the scale $\lambda$ and using $B_\lambda$:

$$P_B(k) = P_B k^\alpha = \frac{2\pi^2\lambda^3 B_\lambda^2}{\Gamma(n_B/2+3/2)}(\lambda k)^\alpha, \qquad (2)$$

where $\lambda$ is a comoving smoothing length (with spatial frequency $k_\lambda = 2\pi/\lambda$), with a Gaussian kernel $\propto \exp[-x^2/\lambda^2]$. For $k > k_D$, where $k_D$ is the cutoff wavenumber, the power spectrum gets dissipated through Alfvén wave damping. The values of $k_D$ for each magnetic field model is given in Tab.1 (8th column).

It is customary to set $\lambda = 1$ Mpc, and therefore in the remainder of the paper we will use $B_{\rm Mpc} = B_\lambda$ to refer to the smoothed magnetic field amplitude.

In Table 1, we provide both the magnetic field settings and the cosmological parameters used in the simulations. The primordial magnetic fields we assume are a bunch of different cases from the range of possible spectral indices, from the almost scale invariant $\alpha = -2.9$ whose energy momentum tensor in Fourier space is infrared dominated, to an high values of $\alpha = 2$ which corresponds to the minimum index allowed for causally generated magnetic fields. The values for the amplitudes of the fields are derived by the constraints with the combination of the most recent data of Planck 2018 (Akrami et al. 2018) with ground based observatory as BICEP/KECK (Ade et al. 2018) and the South Pole Telescope (Keisler et al. 2015) following Paoletti & Finelli (2019) using the gravitational scalar, vector and tensor effects of PMFs on CMB anisotropies.[3] We stress that, in this work, the magnetic seeds used are modelled with configurations, amplitudes and corresponding scale dependences, that are directly derived from CMB data constraints. Concerning the homogeneous field case, we assume a

value of 2 nG in agreement with the COBE constraints (Barrow et al. 1997), that still remain the tightest constraints on homogeneous field from CMB anisotropies. This value is pretty generous and stronger constraints should be provided by Planck in the future, but are not currently available therefore we refer to the COBE ones. Note that the cosmological parameters are not varied for the different settings of the magnetic fields because, as demonstrated by the constraints derived with different observational data and the forecasts for future experiments (Paoletti & Finelli 2011, 2013; Planck Collaboration et al. 2016; Paoletti & Finelli 2019), the inclusion of primordial magnetic fields does not introduce strong degeneracies with the standard cosmological parameters.

We can define an "effective" magnetic field, corresponding to the magnetic energy density generated by the fields above, $B_{\rm eff} = \sqrt{\langle B^2\rangle}$ where the latter is the integrated square magnetic field up to $k_D$ as in Finelli et al. (2008) and Kahniashvili et al. (2013), it can be computed as:

$$B_{\rm eff} = B_{\rm Mpc} \cdot \frac{(k_D\lambda)^{(\alpha+3)/2}}{\sqrt{\Gamma(\alpha/2+5/2)}}. \qquad (3)$$

The $B_{\rm eff}$ corresponding to each model is given in the 10th column of Tab.1: while this is the effective magnetic field value expected if all scales down to $l_D \approx 1/k_D$ can be probed, our simulations can only resolve a larger spatial resolution coarser than $l_D$.

As a consequence, the effective magnetic field amplitude that can be captured by our simulations will be typically smaller that $B_{\rm eff}$. In this work we only consider non-helical magnetic fields. Helical magnetic fields can be generated during inflation Field & Carroll (2000); Vachaspati (2001); Sigl (2002); Sharma et al. (2018) and helicity represent and important component in the evolution of the fields as shown by simulations (Christensson et al. 2001, 2005; Saveliev et al. 2013; Kahniashvili et al. 2017; Brandenburg & Kahniashvili 2017). The helicity impact on CMB anisotropies has been investigated in (Pogosian et al. 2003; Caprini et al. 2004; Kunze 2012; Ballardini et al. 2015; Kahniashvili et al. 2014), and the constraints on the helical field amplitude have beebn explored in (Planck Collaboration et al. 2016). Due to the complexity degree required by the presence of an helical component in the magnetic fields, we leave the helicity treatment for a future work.

Here we impose the initial conditions for the magnetic fields described above at the start of runs, $z_{\rm ini} = 40$. The elapsed time between recombination and $z = 40$ the two epochs is $\approx 65$ Myr, which is negligible compared to the total time of the simulation, and also no significant structure formation is expected to take place in between these two epochs, hence this simplification does not pose any problem for our analysis[4].

We note that in our analysis we consider only the PMFs as a stochastic background with a given a spectral index and an amplitude compatible with the CMB anisotropies constraints, leaving the additional impact of magnetized cosmological perturbations on the matter power spectrum (see for example Sethi & Subramanian 2005; Finelli et al. 2008; Shaw & Lewis 2010; Fedeli & Moscardini 2012; Kahniashvili et al. 2013) for a future work.

Fig. 1 gives the input magnetic power spectra for our models, while Fig. 2 gives the example of the projected maps of magnetic fields strength at $z = 40$ for the B1 ($\alpha = -2.9$) and for the B4 ($\alpha = 1.0$) models. We remark that the variation of the amplitude with the configuration is central for the results we will comment in

---

[3] The additional constraints that are not derived in Paoletti & Finelli (2019) have been computed with the same approach and code as Paoletti & Finelli (2019)

[4] For the current work we do not consider the additional post recombination effect of PMFs.
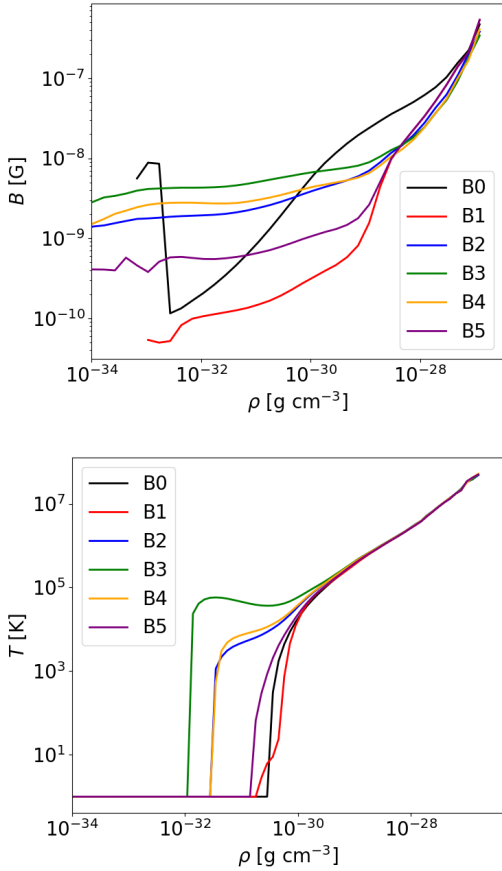
**Figure 4.** Median magnetic field strength as a function of baryon density (top) and median gas temperature for the same gas density bins (bottom) for all models at $z = 0.02$.

the next Sections: spectra which increase the power on the smallest scales are already strongly constrained by the low amplitude of the CMB, whereas fields with more infrared spectra are allowed to larger amplitudes but lower power on much larger scales. The interplay between the scale dependence of the fields, and the constraints on their amplitude by the CMB, will be reflected into the lower redshift constraints explored in the rest of this work.

## 3   RESULTS

### 3.1   Properties of simulated magnetic fields

#### 3.1.1   Global properties

The panels in Fig. 3 show the spatial distribution of our simulated magnetic fields, for all models, at $z = 1$ and $z = 0.02$.

As expected, large differences are present at all epochs, outside of collapsed matter halos in the volume. The amplitude of magnetic fields in the mildly dense (e.g. sheets/filaments) and underdense (e.g. voids) cosmic environment are found to vary by $\sim 10 - 10^2$ depending on the seeding model, event by the end of the simulation $z = 0.02$. The magnetic field amplitude within halos is instead almost exactly the same in all cases, owing to our subgrid dynamo model, whose key ingredient is the small-scale gas kinetic energy, which is basically identical in all runs.

In Fig. 4 we quantify the typical magnetic field level (and tem-

perature) as a function of gas density. We can notice significant differences among models at low densities, $\rho \leqslant 10^{-29} \mathrm{g/cm^3}$, i.e in the environment of the outer regions of halos, or even outside them. In voids, there is a $\geqslant 10$ difference in magnetic field intensity between models. While in the simple uniform seeding model (B0), the magnetisation is a strong function of gas density, in most of the other models the presence of initial large fluctuations in the seed fields produces a broader distribution of magnetic fields in voids, smoothing out any strong dependence with density.

A new finding of our analysis is the presence of differences in the average *gas temperature* in voids ($\rho \sim 10^{-32} - 10^{-31} \mathrm{g/cm^3}$), depending on the magnetic seed model. For example, in models B2, B3 and B4 the average temperature of voids can reach $\sim 10^2 - 10^3$ K, i.e. much beyond the $\leqslant 10$ K of the standard B0 run here. Both temperatures are unrealistic, in the sense that the reheating from reionization (which would rise the gas temperature to $\sim 10^3 - 10^4$ K everywhere, Haardt & Madau 1996) is completely missing in these models. However, such differences are significant and hint at a substantial extra heating that primordial magnetic field fluctuations are introducing. Large initial fluctuations of magnetic field can become relevant for the local gas dynamics, because via induction equation they can trigger the formation of shock waves and the dissipation of turbulent motions into heat, in way qualitatively similar to what has been proposed during recombination epochs (e.g. Trivedi et al. 2018; Jedamzik & Saveliev 2019). Also post-recombination, dissipative effects on the magnetic fields as MHD decaying turbulence and ambipolar diffusion, whose study is currently based mainly on approximated linear numerical treatments, show similar levels of the heating of the plasma (Kunze & Komatsu 2015; Chluba et al. 2015; Paoletti et al. 2019). The development of extra shocks for gas with $\rho \leqslant 10^{-31} \mathrm{g/cm^3}$ is well captured by the $(\rho, \mathrm{T})$ phase diagrams of Fig. 5, in which we also computed the dissipated energy flux through shocks identified in the simulation [5]. The additional shocks in empty regions stand out in the statistics of detected shocks in the left part of the phase diagrams, well away from the typical regime of structure formation shocks driven by gravity (e.g. Vazza et al. 2011).

We remark that such new classes of shocks driven by magnetic fields may not be physically very relevant, because of the aforementioned lack of a reionization heating floor in our model, as well as because the energy flux associated with such shock is extremely small, i.e. $\leqslant 10^{-7}$ of the total energy dissipation of kinetic energy in the total cosmic volume.

However, the exact topology of magnetic fields in the volume swept by cosmic shocks is also relevant as it can affect the acceleration efficiency of cosmic rays (CR). Protons and/or electrons should undergo different kinds of shock acceleration as a function of plasma parameters as well as of the topology of up-stream magnetic field (e.g. Bykov et al. 2019, and references therein for a recent review). While CR protons should be efficiently accelerated by strong shocks with a quasi-parallel geometry between the shock normal and the upstream magnetic field via Diffusive Shock Acceleration (DSA), CR electrons may be accelerated in a two-phase fashion, in which they first gain energy via shock-drift acceleration if shocks are quasi-perpendicular, and are later suitable for acceleration by DSA (e.g. Caprioli & Spitkovsky 2014; Guo et al. 2014).

---

[5] Shocks are identified in post-processing, with a velocity-based scheme to compute the Mach number based on jumps of thermodynamical quantities, as in Vazza et al. (2009) and Banfi et al. (2020)
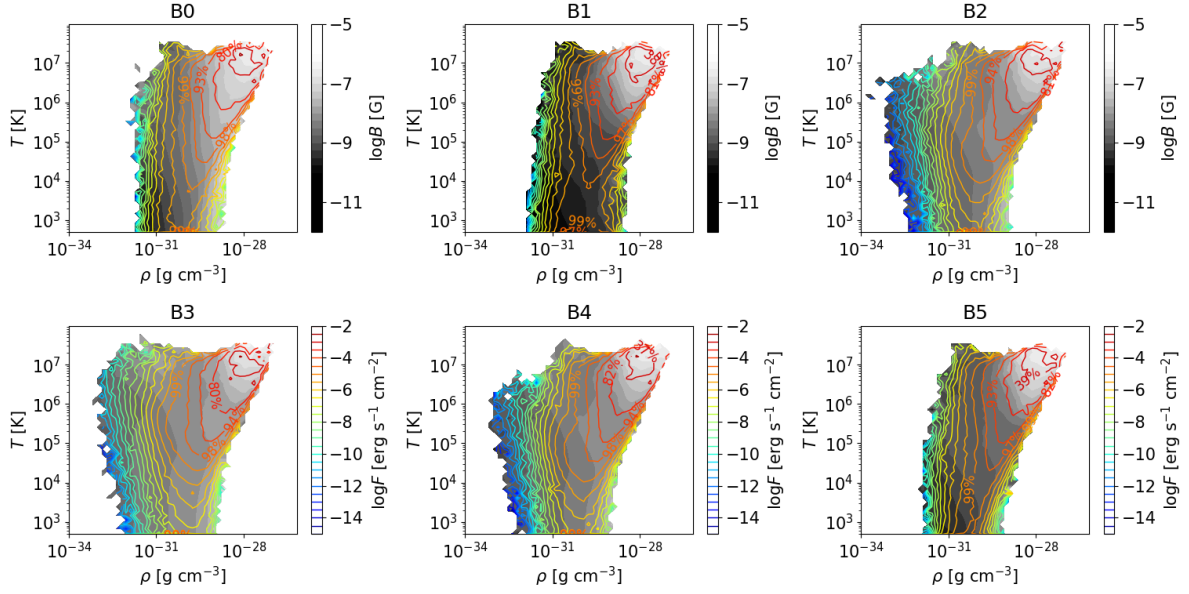
**Figure 5.** Phase diagrams of baryons in all simulations at $z = 0.02$. The additional color coding gives the median magnetic field strength in each gas phase (BW color palette) and the total dissipated energy flux at shocks (contours).
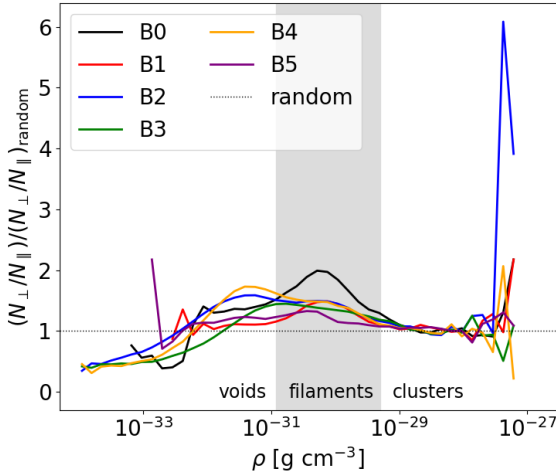


**Figure 6.** Distribution of the ratio quasi-perpendicular to quasi-parallel shocks, normalised to the expected ratio in a random 3-dimensional distribution, a function of gas density at $z = 0.02$.

Following Banfi et al. (2020), we measured the shock obliquity from the shock propagation direction and the up-stream magnetic field $\boldsymbol{B}$: $\theta = \arccos\left(\frac{M_x \cdot B_x + M_y \cdot B_y + M_z \cdot B_z}{M\, B}\right)$ which ranges from $0°$ to $180°$. For the identification of up-stream magnetic field values and of the local shock propagation direction, we rely on our velocity-based shock finder (Banfi et al. 2020).

Fig. 6 shows the ratio between quasi-perpendicular ($|\theta| \geqslant 45°$) and quasi-parallel ($\theta < 45°$) for all models as a function of the gas density, normalized to the ratio that is expected from a purely random distribution of vectors in 3D space (which follows a simple $\propto \sin\theta$ probability distribution).

All models present an excess of quasi-perpendicular shocks, with respect to a random distribution, in the broad range of den-

sities $\rho \approx 10^{-32} - 10^{-29}$ g cm$^{-3}$. The excess is maximal at the overdensity typical of filaments, which is explained by the fact that filaments tend to stretch the local magnetic field perpendicular to the velocity shear and to the local density gradient (Soler & Hennebelle 2017), while shocks are mostly running along the density gradient (Banfi et al. 2020). Therefore, in all models filaments of the cosmic web are an environment in which the acceleration of CRs mostly proceed via quasi-perpendicular shocks, which would correspond to a reduced injection of CR protons in such structures (see Wittor et al. 2020; Banfi et al. 2020, for recent detailed analysis).

However, quantitative differences in the excess of quasi-perpendicular shocks can be seen, with the highest excess being present in the uniform B0 model. This can be understood in terms of magnetic *tension*, i.e. of the difficulty by the gas flow in bending magnetic field lines. The tension increases with the field curvature, hence it is not surprising that in the B5 model, where the initial tangling of magnetic field lines is maximal at small scales, the gas dynamics struggle more than in the B0 case to bend the field direction and align it perpendicular to the gas density gradient. Intermediate trends are found in all other models. As an effect of small-scale dynamo in halos, all these effects are erased for $\rho \geqslant 10^{-28}$ g/cm$^3$, and the distribution of shock angles gets consistent with a purely random distribution (e.g. Wittor et al. 2017b).

Next, we measure the global volumetric and topological properties of magnetic fields for different epochs through their Probability Distribution Functions (PDF) and their 3-dimensional power spectra, as shown by Fig. 7- 8, where we considered three evolutionary steps as an example: $z = 5, 0.4$ and $0.02$.

In the PDF, large differences are seen at all epochs, with the tendency to similarity of all models in the high magnetisation regime ($\geqslant 0.1\ \mu G$) and for $z \leqslant 1$, after the small-scale dynamo has started operating in most halos. However, for the bulk of the volume of the cosmic web the relative differences in the peak of the PDF
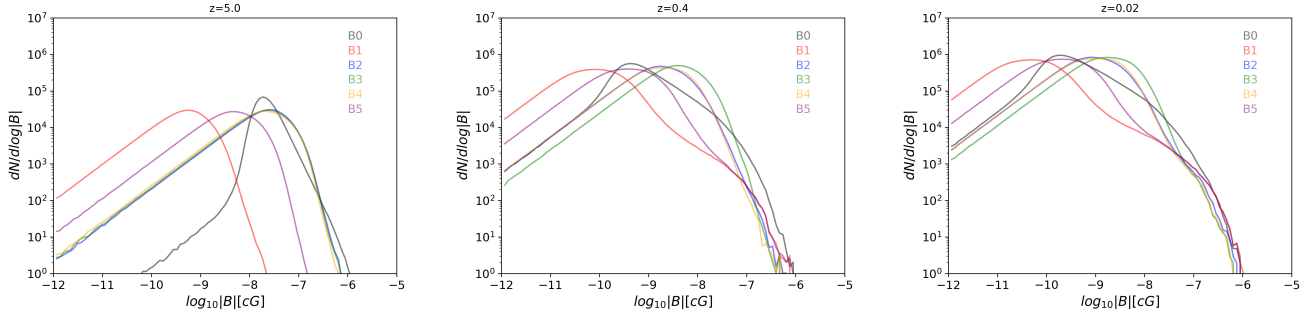
**Figure 7.** Probability distribution functions of comoving magnetic field strength for our models at four different epochs.
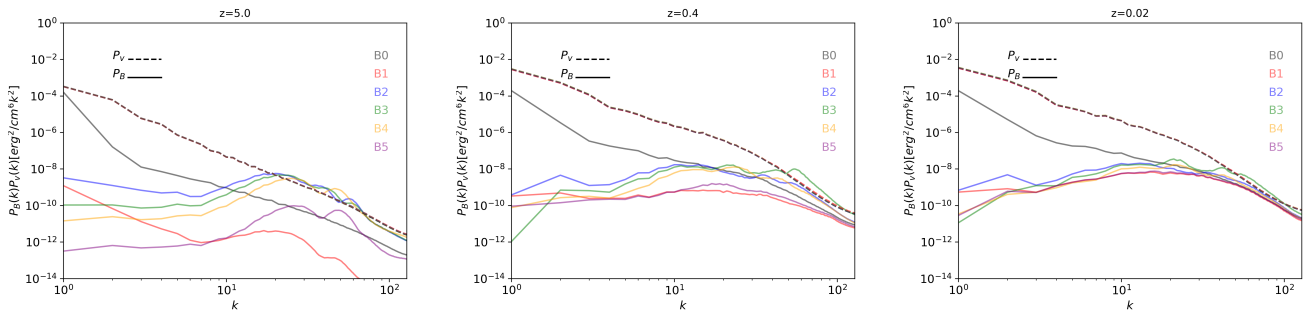


**Figure 8.** 3-dimensional magnetic power spectra (solid lines) and kinetic energy spectra (dashed lines) for our models at four different epochs.
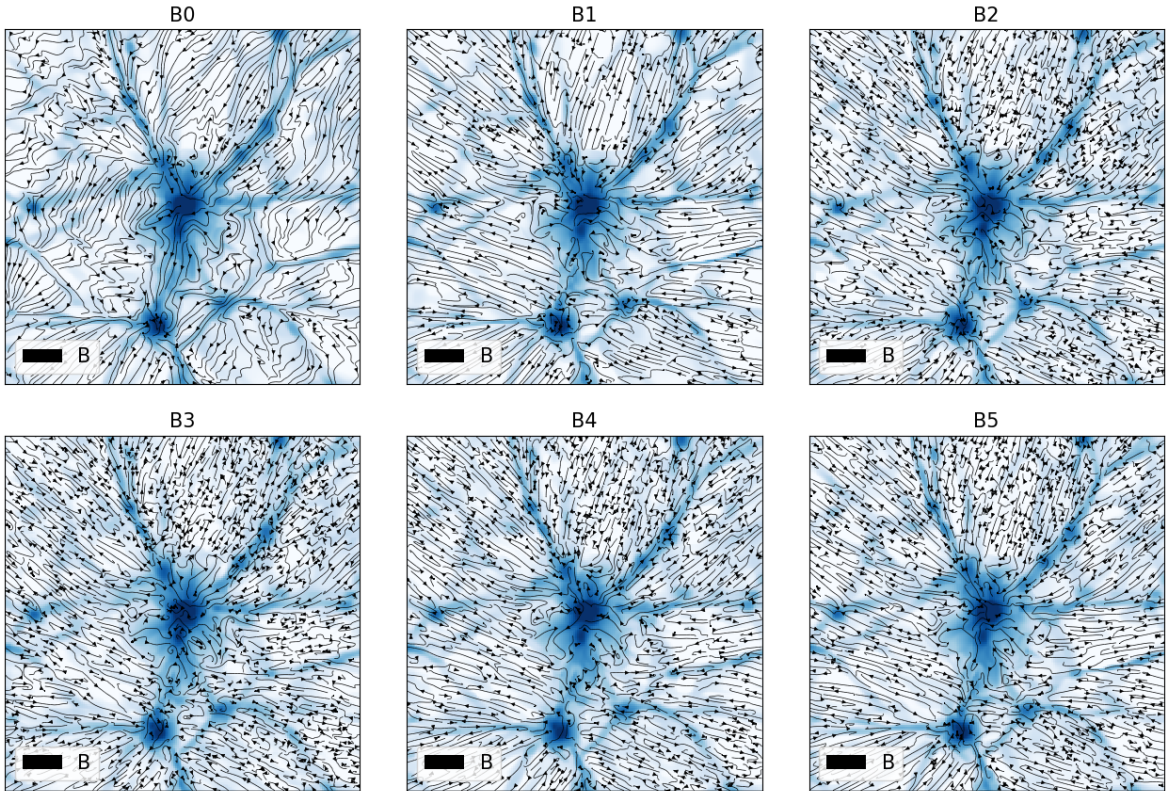


**Figure 9.** Thin slices (195 kpc thick) showing the gas density (blue) and the magnetic field lines (black) for a $20 \times 20$ Mpc$^2$ zoom around the most massive cluster in our simulated volume at $z = 0$.

are preserved from $z = 5.0$ to $z = 0.02$, and they mirror the differences at $z = 40$, suggesting that in all cases the overall evolution of the PDFs is mostly driven by compression-rarefaction. This further supports that, at least in theory, it should be possible to constrain the magnetisation model of our Universe, provided that we can probe the volumetric distribution of extragalactic magnetic fields today.

We computed the power spectra with standard Fast Fourier Transform techniques on the 3-dimensional grid, assuming periodicity, and in the case of the velocity spectrum, $P_v(k)$, we weighted the velocity variable by the square root of gas density, $v' = \rho^{1/2}v$, so that the kinetic and magnetic spectrum, $P_B(k)$, have the same units. $P_v(k)$ is indistinguishable in the six runs, indicating that differences in the magnetic field at the level explored in this work cannot affect the overall gas kinematics in any important way. On the other hand, the evolution of $P_B(k)$ shows substantial differences on all scales for $z \geqslant 1.0$, while at lower redshift the spectra overlaps on scales $\leqslant 10 - 20$ Mpc, as a result of the dynamo amplification. The similarity between models at small spatial scales is driven by our subgrid dynamo model. Since the small-scale dynamo erases any topological memory of initial fields in the real Universe (e.g. Cho 2014; Marinacci et al. 2015; Vazza et al. 2018), all models look alike. Already from this test, it is clear that the differences between models at low redshift will be minute and difficult to observe, because most of the difference is contributed by very large spatial scales, $\gg 10$ Mpc, which are characterised by low densities and large angular scales in the sky.

### 3.1.2 Properties of galaxy clusters

We first examine the properties of our simulated population of galaxy clusters and groups, in order to check whether significant differences between extreme variations in the primordial seed fields can already be detected.

First, we identified galaxy clusters in our runs, using a standard algorithm based on the spherical (gas+DM) overdensity (e.g. Gheller et al. 1998), and extracted the total mass and average (volume weighted) magnetic field strength within $R_{200}$, i.e. within the radius enclosing a matter density 200 times the cosmological critical density.

In principle, the presence of a large magnetic tension in the cosmological initial conditions may induce a change in the late evolution of the clustering properties of galaxy clusters, of their mass function as well as of their thermal scaling relations (e.g. Dolag et al. 1999, 2001; Kahniashvili et al. 2013; Sanati et al. 2020). However, the top panel of Fig. 10 shows that the mass function of halos identified in all simulations at $z = 0.02$ are basically indistinguishable, across more than two orders of magnitude in mass, down to $\approx 10^{12} M_\odot$. Moreover, the scaling relations between the cluster mass and the average gas temperature within $R_{200}$ show no differences (not shown).

On the other hand, larger differences are measured for the average (volume weighted) magnetic field strength within $R_{200}$, $\langle B_{200} \rangle$, between the same objects. The best-fit relations given in the lower panel of Fig. 10 suggest that the differences are on average of order $\leqslant 10 - 20\%$ between extreme models. This makes the detection of any difference on these small scales extremely challenging, because in observations the global cluster magnetic field can be either estimated through the (sparse) sampling of Faraday Rotation from background polarised sources, and/or from the modelling of diffuse radio emission originating from shocks or turbulence (e.g. Brunetti & Jones 2014; van Weeren et al. 2019). Therefore, we consider any differences of the magnetic field distribution inside
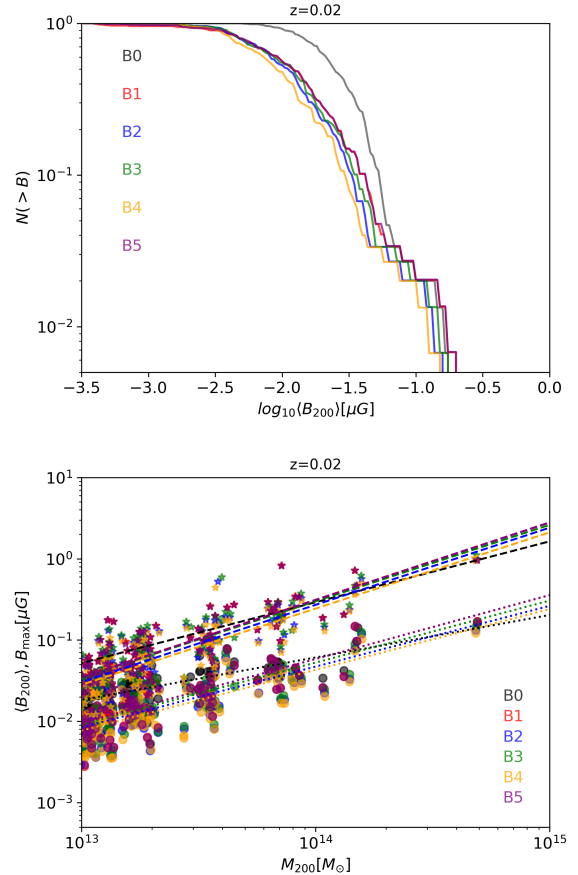


**Figure 10.** Top: cumulative mean magnetic field strength (volume averaged within $R_{200}$) for the same halos. Bottom: scatter plot relating $M_{200}$ and the average ($\langle B_{200} \rangle$) or the maximum ($B_{max}$) magnetic fields for the same clusters. The additional dashed/dotted lines gives the best fits of the two relations.

clusters or groups of galaxies likely too weak to be detectable by observations.

Unlike in Kahniashvili et al. (2013), we consider only the stochastic background of primordial magnetic fields and do not account for the effect of magnetized perturbations on the matter power spectrum at small scales. For this reason, the effects of different models on the final distribution of cluster masses might be underestimated. However, even in the more self-consistent (analytical) work by Kahniashvili et al. (2013), significant effects of primordial magnetic fields on the halo mass function are confined to $\leqslant 10^{12} M_\odot$ halos for most models, i.e. in a range of masses which cannot be properly resolved by our runs here. In particular, Kahniashvili et al. (2013) reported that the number of small mass objects ($M \sim 10^4 M_\odot$) in the most magnetised cases can be reduced by a factor $\sim 10^2$ compared to the unmagnetised case number, while an excess in the number halos with respect to the unmagnetised case is found for objects with masses of $\sim 10^{10} M_\odot$.

## 3.2 Observable properties

We compute the *Faraday Rotation Measure* (RM) across the full length of the simulated box, by integrating for each 1-dimensional beam of cells the quantity:
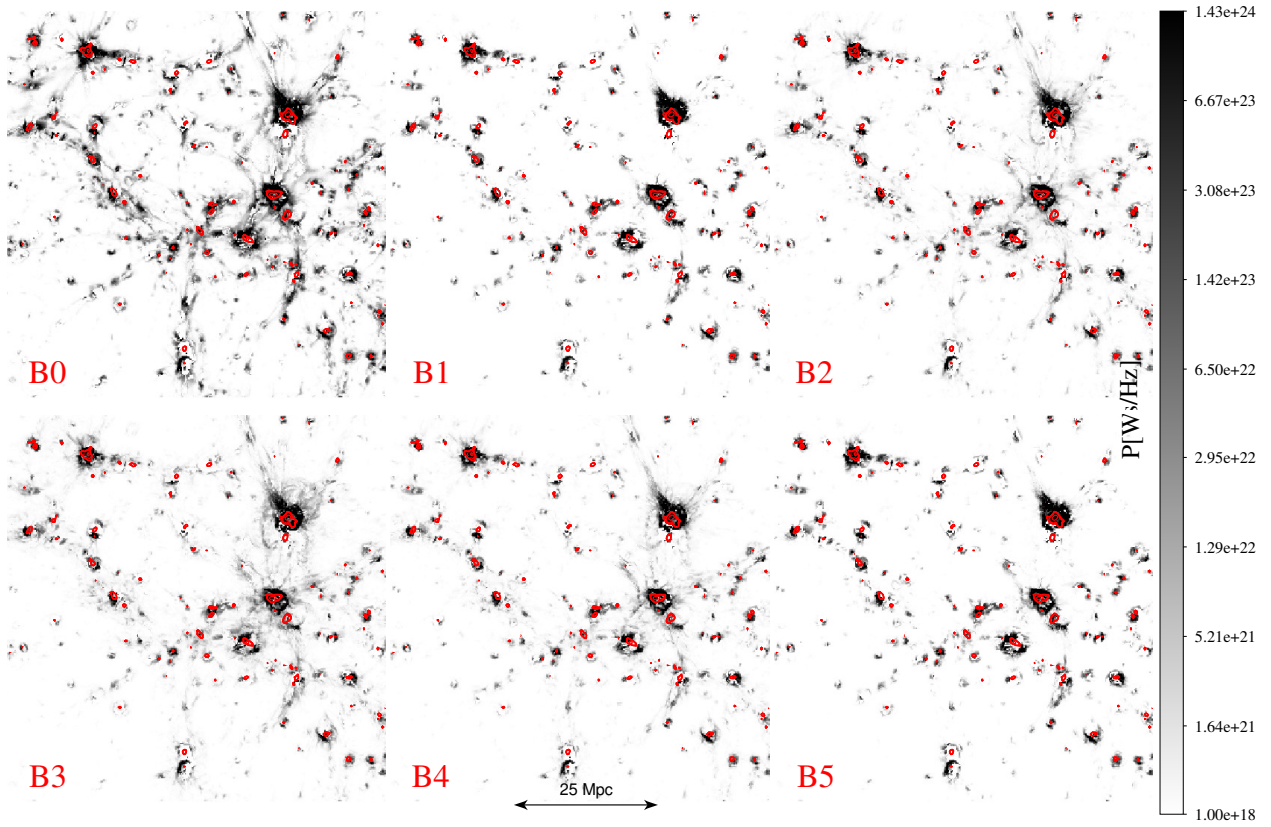
**Figure 11.** Synchrotron radio emission ($\nu = 100$ MHz) from cosmic shocks along the entire 100 Mpc, and projected DM density (red contours) for all our models at $z = 0$.
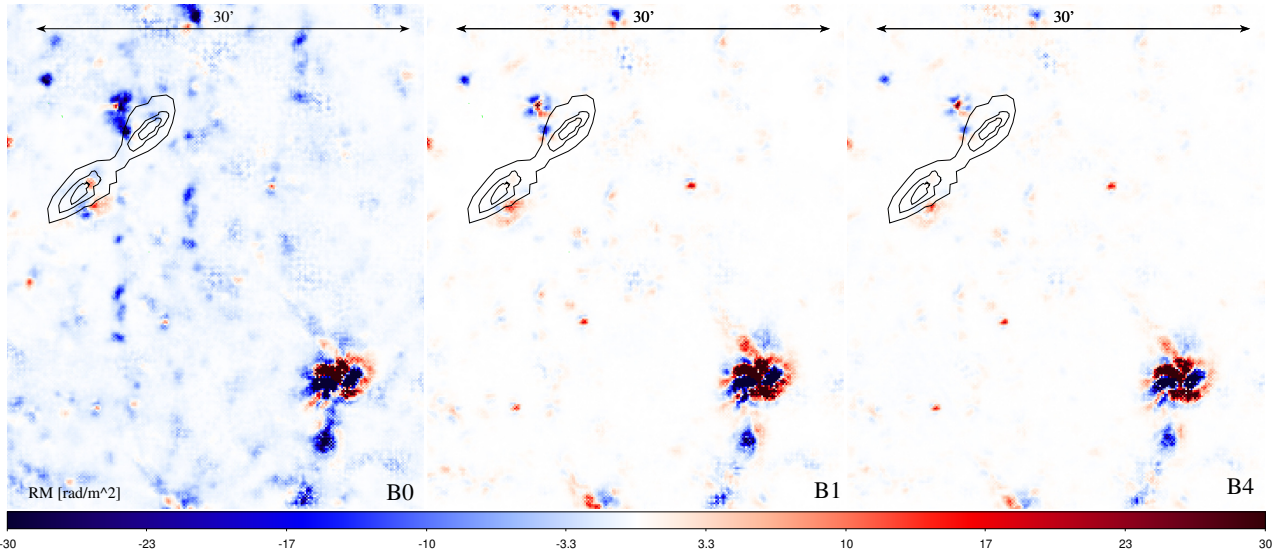


**Figure 12.** Integrated Faraday rotation for a $\sim 30' \times 50'$ field of view with depth until $z = 0.5$, for models B0, B1 and B4. The maps are convolved for a 20" resolution beam. The simple sketch of an FRII radio galaxy is added to refer to our analysis discussed in Sec.3.2.1.

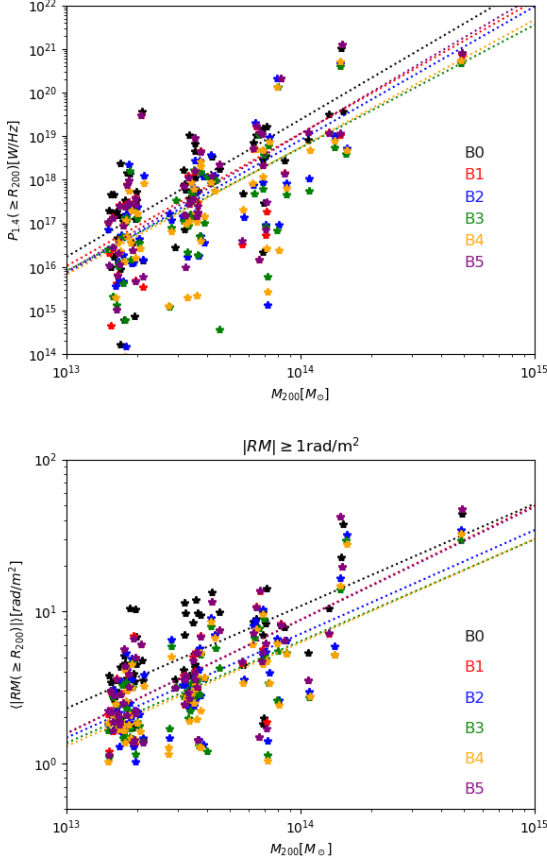**Figure 13.** Top: radio power from shocks at 1.4 GHz from peripheral, $R_{200} \leqslant r \leqslant 2R_{200}$ regions vs $M_{200}$ at $z = 0.02$ for the same clusters in all runs. The dotted lines show the best fit relations for each model. Bottom: average $|RM|$ in the range $R_{200} \leqslant r \leqslant 2R_{200}$, considering a (future) $|RM| \geqslant 1$ rad/m$^2$ sensitivity. The dotted lines show the best fit relations for each model.
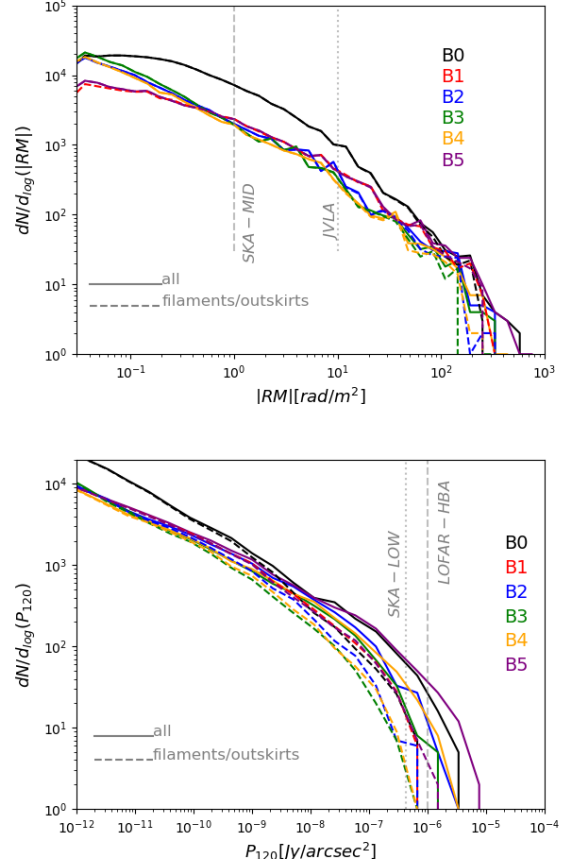
**Figure 14.** Top: distribution functions of Faraday Rotation for all models and a $2° \times 2°$ field of view up to $z = 0.8$. Bottom: distribution function of synchrotron radio emission at 1.4 GHz for all models and a $2° \times 2°$ field of view up to $z = 0.8$.

$$\frac{R}{[\mathrm{rad/m}^2]} = 812 \int \frac{B_{||}}{[\mu G]} \cdot \frac{n_e}{[\mathrm{cm}^3]} \frac{dl}{[\mathrm{kpc}]} \frac{1}{1+z}, \tag{4}$$

in which $B_{||}$ denotes the component of the magnetic field parallel to the line of sight (LOS), $z$ is the redshift of each cell, $n_e$ is the physical electron density of cells, assuming a primordial chemical composition of gas matter everywhere in the volume ($\mu = 0.59$). RM thus corresponds to the Faraday Rotation experienced by sources of linearly polarised radio emission, located in the background of our LOS.

To compute the diffuse *synchrotron radio emission* from the cosmic web, we limit here to the contribution from cosmic shocks (e.g. Vazza et al. 2015) and assume that relativistic electrons get accelerated by DSA. We closely follow the formalism by Hoeft & Brüggen (2007), and compute the synchrotron emission for each shocked cell (identified with a velocity-based approach as in Vazza et al. 2009) as the convolution of the several power-law distributions of electrons that overlap in the cooling region downstream of each shock:

$$\frac{P(\nu)}{[\mathrm{erg/s/Hz}]} = 6.4 \cdot 10^{34} \cdot \int \frac{\xi_e(\mathcal{M}) \cdot A}{\mathrm{Mpc}^2} \frac{n_e}{10^{-4}\mathrm{cm}^{-3}}$$

$$\left(\frac{T}{7\mathrm{keV}}\right)^{3/2} \left(\frac{\nu}{\mathrm{GHz}}\right)^{-s/2} \cdot \frac{B^{1+s/2}}{B_{\mathrm{CMB}}^2 + B^2} \frac{1}{(1+z)^2} dV, \tag{5}$$

in which $A$ is the shock surface, $T$ is the cell temperature, $s$ is the energy spectrum of accelerated particles, defined as $s = 2(\mathcal{M}^2+1)/(\mathcal{M}^2-1)$, $B$ is the magnetic field (in $\mu G$ and $B_{\mathrm{CMB}}$ is the CMB-equivalent magnetic field. $\nu$ is the observing frequency, $dV$ is the cell volume and $\xi_e(\mathcal{M})$ is the acceleration efficiency of electrons, which is $\leqslant 10^{-4}$ for weak shocks ($\mathcal{M} \leqslant 3-4$) and it reaches $\sim 10^{-2}$ for strong, $\mathcal{M} \gg 10$ shocks.

The panels in Fig. 13 give the distribution of RM and of radio power for all galaxy clusters in our volume, limited to their peripheral $\geqslant R_{200}$ regions, which are the typical location of peripheral radio relics (van Weeren et al. 2019).

The best-fit relations for the relation between the radio emission or the Faraday Rotation and $M_{200}$ of halos have quite similar slopes, while their differences in normalisation follow from the different trends in the average magnetic field found in Fig. 10. Interestingly, this suggests that already outside of $R_{200}$ there is a residual difference in radio observables, that is not entirely erased by the action of the small-scale dynamo amplification. A higher value of RM and synchrotron emission is expected for the simple B0 model, consistent with the systematically higher average fields found in the previous Section. However, the scatter present in both quantities within all mass bins is much larger than the difference between
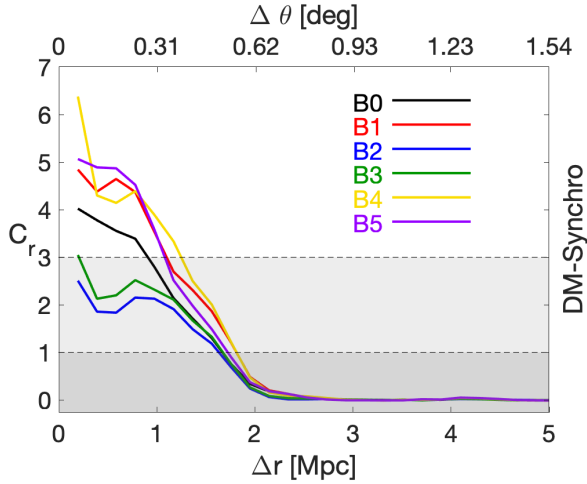
**Figure 15.** Simulated cross-correlation between the projected dark matter distribution (simulating galaxies) and the synchrotron emission detectable by MWA, using the observing configuration by Vernstrom et al. (2019). The cross-correlation is normalised to the corresponding null model and the horizontal lines mark the 1 and 3 $\sigma$ detection level.

models. Because of this, only with very large surveys of clusters it might be possible to reduce the effect of cosmic variance, which are instead a big limitation with samples of $\leqslant 50$ objects as the one simulated here.

### 3.2.1 Cosmological light cones

In the remainder of the paper, we consider the integrated synchrotron radio emission or Rotation Measure from light cones which are longer than our simulated volume, in order to produce a more realistic match with what observations can do. In detail, we used stacked 10 different redshift snapshots for each of our model resimulations, by extracting a corresponding carrot within a fixed aperture ($\theta = 2°$). The light cone was build by adding the information within each volume at regular intervals of 100 Mpc (comoving) along the line of sight, and by introducing random shifts across the plane of the sky to avoid repeating patterns, until producing a $0.02 \leqslant z \leqslant 0.8$ light cone.

The panels in Fig. 14 give the distribution of synchrotron radio emission (at $\nu = 1.4\,\mathrm{GHz}$), and of Faraday Rotation for background polarised sources for all our models. We additionally mark the regions traced by "filaments" based on the projected mass-weighted gas temperature, using a fiducial threshold of $T_{\mathrm{fila}} = 10^7\,\mathrm{K}$ to disentangle the signal produced by halos from the one produced by more rarefied regions.

Small, but non negligible differences, appear between different models, albeit in a regime which is challenging to observe with current instruments. There is a level of difference from filaments in the cosmic web (dotted lines), which seems to be at the edge of detectability both in Faraday Rotation and in synchrotron emission. It is also worth noticing that there is a systematic difference in Faraday Rotation between a simplistic uniform primordial magnetic field model (B0) and all other models. The B0 model yields a $\sim 3 - 5$ higher Faraday Rotation for filaments, compared to all other models, consistently our previous results on clusters, and following from the fact that the rather laminar magnetic field lines in the bulk of cosmic volume do produce a systematic Faraday Rotation of background sources.

### 3.2.2 Comparison to available radio observables

A few authors have claimed a derivation of upper limits on the average magnetisation of the cosmic web, based on the statistical analysis of radio surveys (e.g. Vernstrom et al. 2017, 2019; O'Sullivan et al. 2020). Our simulations can already be used for a first tentative comparison with recent work, albeit within the caveat posed by their limited resolution, which are discussed in detail in Sec.4 and in the Appendix.

First, we attempt a qualitative comparison with the recent results by Vernstrom et al. (2017), who have cross-correlated the MWA Phase I radio observations and the large-scale distribution of galaxies observed with the WISE+2MASS galaxy survey, for a $22° \times 22°$ field of view. Vernstrom et al. (2017) reported no significant detection of cross-correlation between galaxies and radio emission on $\geqslant 20'$ scales, and used this information to derive upper limits on the typical magnetisation of filaments of the cosmic web. In Gheller & Vazza (2020) we introduced a procedure to simulate the the cross-correlation between the diffuse radio emission at 180 MHz and the projected galaxy distribution in the simulation. In particular, we set the threshold of projected DM density to $\rho_{th} = 6 \cdot 10^{-29}\,\mathrm{g/cm^3}$ in order to produce a number of galaxies (i.e. dark matter halos) compatible with the sensitivity of the WISE IR survey, yielding $\sim 10$ galaxies per square degree for $z \leqslant 0.07$ (Vernstrom et al. 2017). For the radio emission, we considered the MWA Phase I sensitivity and resolution beam as in Vernstrom et al. (2017), by convolving our radio sky model for a $\theta \approx 2.9'$ resolution beam and considering a (spatially uniform) noise level of $0.96\,\mathrm{mJy/beam} \approx 0.028\,\mu\mathrm{Jy/arcsec^2}$ at 180 MHz.

Following Gheller & Vazza (2020), the normalised correlation matrix $C$ between 2D $N \times M$ pixels images $A$ and $B$ is evaluated through:

$$C(k,l) = \frac{1}{NM} \sum_{j=0}^{N-1} \sum_{i=0}^{M-1} \frac{(A(i,j) - \bar{A})(B(i+k,j+l) - \bar{B})}{\sigma_A \sigma_B}, \qquad (6)$$

where $\bar{A}$ and $\bar{B}$ are the mean values of the two images and $\sigma_A$ and $\sigma_B$ are their standard deviation, while the indices of the correlation matrix $C$ give the shift (displacement) of the two images. The significance of the cross-correlation is evaluated against the case of null correlation, for which $C$ is computed between $A$ and $B$ from uncorrelated $50 \times 50\,\mathrm{Mpc^2}$ sub-tiles extracted from the main simulation.

The results are shown in Fig. 15; they cannot be readily compared with the cross-correlation values given by Vernstrom et al. (2017), owing to the different approaches in estimating the noise level of the cross-correlations. Therefore, our synthetic observation can only qualitatively address which model seems to be more compatible with MWA observations. While all models give a significant cross-correlation out to $\sim 40 - 50'$, the amplitude of the correlation in the B1, B4 and B5 models (and, to a smaller extent, over the homogeneous B0 model) seems to be too large to have been missing missed by MWA observations. This potentially suggests already that a 1 nG initial field (resulting into a typical magnetisation of filaments of $10 - 100$ nG as shown in Gheller & Vazza 2019) is too large to be compatible with the lack of detection reported by Vernstrom et al. (2017). Interestingly, intermediate models B2 and B3 present cross-correlation only at the $\leqslant 2\sigma$ level and on slightly smaller angular scales.

As a caveat, given the finite mass resolution of our simulations, we cannot properly form dwarf galaxies in voids (or in very poor environment, in general). Therefore, even if the number of galaxies is calibrated to be at the level of the galaxy distribution

observed in WISE/MASS surveys, our spatial distribution is typically more clustered than in observations. In principle, this can decrease the cross-correlated signal coming from low density regions in our sample. With future work, we will employ more resolved simulations in order to address this issue.

O'Sullivan et al. (2020) recently reported limits on the Faraday depth contribution of the magnetised cosmic web, by comparing the structure function of Faraday Rotation in random pairs of radio galaxies compared to physical radio galaxies (i.e. doubled-lobed radio galaxies), on overlapping angular scales.

We produced mock structure functions of Faraday Rotation for our simulated deep light cones, following the same procedure as in O'Sullivan et al. (2020). We integrated the RM along the line of sight down to $z = 0.7$, and computed the statistic of $\langle (\Delta RM)^2 \rangle$ for physical pairs of pixels, by placing pairs of sources at regular intervals of 100 Mpc (comoving) along the line of sight (i.e. at the end of each of the comoving volumes used to produce the stacking sequence of Faraday Rotation). In detail, we first randomly drew $20,000$ sources (with $|RM| \geqslant 0.03$ rad/m$^2$ as in the LOFAR observation, for 10 evenly spaced redshift bins, and calculated $(\Delta RM(\Delta\theta)^2)$ at each redshift. The assumed angular resolution for the light-cone of Faraday Rotation is the same of O'Sullivan et al. (2020) LOFAR-HBA observation, i.e. $\approx 20$". The final distribution of $(\Delta RM(\Delta\theta)^2)$ can be compared with recent LOFAR-HBA observations by O'Sullivan et al. (2020), by weighting each structure function in redshift bins for the (likely) redshift distribution function of sources, derived in Vernstrom et al. (2019).

Fig. 16 gives the simulated distribution of $(\Delta RM(\Delta\theta)^2)$ as a function of angular separation for all our models, compared with real LOFAR-HBA data (grey area). At the face values, the structure functions of models B1 and B5 appear strongly disfavoured by the comparison with observations, while all other models remain compatible with LOFAR data, even if it is non trivial to evaluate the uncertainties in the signal from simulations, owing to the limited volume scanned here as well as to the different selection function of sources in redshift applied to simulated data. The trend for B1 and B5 is in striking good agreement with the previous test on the cross-correlation of synchrotron emission and the galaxy distribution, in the sense that these two models already likely to ruled out by radio observations. However, our limited spatial resolution is likely to underestimate the Faraday structure below $\leqslant 200$ kpc, with a stronger effect than in the case of synchrotron emission, because Faraday Rotation is more sensitive to the (unresolved) small-scale topology of magnetic and density perturbations. We comment on this issue more in detail in Sec. 4 and in the Appendix. Moreover, it is important to notice that the above structure functions still have an unknown contribution from the Rotation Measure variance of the Milky Way. In case this is dominant on $\leqslant 10'$ scales, the observational constraints from $(\Delta RM(\Delta\theta)^2)$ will decrease to lower values, possibly putting tension on all models investigated here.

### 3.2.3 The deflection of Ultra-High-Energy Cosmic Rays

Finally, we investigated whether the propagation of Ultra-High-Energy Cosmic Rays across cosmic distances is differently affected by our different magnetic field models. Cosmic rays with energies $\geqslant 10^{18}$ EeV are indeed believed to have a predominantly extragalactic origin, and their propagation towards Earth must be deflected by the Lorentz force by extragalactic magnetic fields (e.g. Sigl et al. 2003; Dolag et al. 2005). Large deflections hamper the possibility of locating the real sources of UHECRs at the highest energies(e.g. Biermann et al. 2016), yet the amplitude of these de-
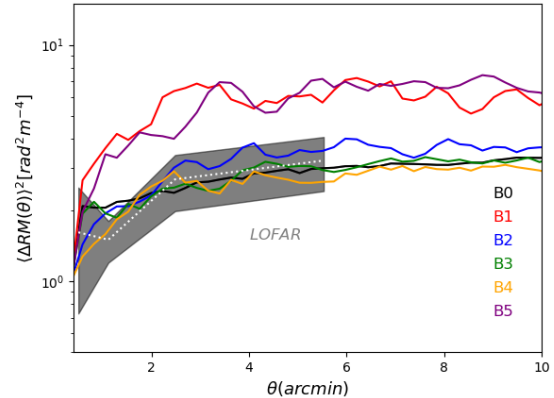


**Figure 16.** Simulated distribution of $(\Delta RM(\Delta\theta)^2)$ as a function of angular separation for all our models. The grey area shows the LOFAR 144 MHz data by O'Sullivan et al. (2020), with noise power from measurement errors subtracted, for physical pairs of radio sources only.

flections can greatly vary depending on model assumptions, ranging from $\leqslant 1°$ to $\sim 30°$ (e.g. Dolag et al. 2005; Berezinsky 2014; Alves Batista & Sigl 2014). We recently studied the propagation of UHECRs in *ENZO* simulations combined to the CRPropa code (Alves Batista et al. 2016), finding that the observed level of isotropy of $\geqslant 10^{18}$eV UHECRs rules out primordial models with a uniform magnetic field larger than $\sim 10$ nG (Hackstein et al. 2016, 2019).

The typical deflection angle, $\theta$, of a cosmic ray of energy $E$ and charge $Z$ propagating through the extragalactic magnetic field can be simply estimated as

$$\theta(E) = 0.8 \, Z \left( \frac{E}{10^{20}\text{eV}} \right)^{-1} \cdot \left( \frac{r}{10\text{Mpc}} \right)^{1/2} \cdot \left( \frac{\lambda_B}{\text{Mpc}} \right)^{1/2} \cdot \frac{B}{\text{nG}} \qquad (7)$$

where $\lambda$ is the typical coherence length of magnetic fields (assumed in this case to be constant across the cosmic volume, and fixed to $\lambda_B = 1$ Mpc here for simplicity), and $r$ is the propagation length (e.g. Sigl et al. 2003).

The maps in Fig. 17 give a visual impression of the average deflection angle computed from the above formula, for runs B0, B1 and B4 at $z = 0.02$. Very large ($\theta \gg 10°$) deflection angles are expected for UHECR protons crossing the virial regions of halos, due to the $\geqslant 0.1 \, \mu$G field developed there. In the case of the uniform B0 model however the deflection is significant in filaments too, and far from negligible for the entire projected sky ($\theta \sim 10°$). Deflections are still non negligible in the B5 model ($\theta \sim 2°$), while in the model B1 the deflection is almost negligible ($\theta \leqslant 1°$) for most of the projected area, once halos are excluded.

A proper simulation of the effect of deflection by extragalactic magnetic fields requires to properly integrate the trajectories of cosmic rays crossing our simulated volume. We thus simulated the propagation of UHECRs by integrating the trajectories of 2000 randomly distributed cosmic rays for each model, assuming a random initial orientation of their velocity (which is of course $|v| = c$) and we integrated their propagation through the simulated $100^3$ Mpc$^3$ volume in all models. In detail, their propagation was integrated by computing the deflection by the Lorentz force with a kick-drift-kick second-order integration scheme (e.g. Ryu et al. 2010), assuming that all cosmic rays are protons ($Z = 1$) with an initial energy of $10^{18}$eV, $10^{19}$eV or $10^{20}$eV, and neglecting all other loses of energy

via other processes, which is a reasonable enough assumptions considering the relatively small propagation length considered here. The maps in Fig. 18 show the paths of a sample of protons through runs B0, B1 and B5, while in Fig. 19 we give the distributions of deflection angles for the protons with the three possible initial energies, by computing $\theta$ as the angle between the initial injection direction and the final velocity vector, either after 30 or 100 Mpc of propagation length since their origin. Consistent with the expectations of deflection angles, we observe a large difference in the typical propagation of UHECR protons in the B0, B1 and B5 case. The largest deflection is measured in the B0 scenario, in which the distribution of directions of UHECRs of $10^{20}$eV gets entirely randomized after propagating for $\sim 100$ Mpc. For most of observers in this simulated Universe it will be thus entirely impossible to track the origin of received UHECRs, backwards to their original injection location. In most investigated models, already after $\sim 30$ Mpc of propagation the observed UHECR protons (for $E \leqslant 10^{20}$eV) are so highly deflected, that that "UHECRs astronomy" would impossible. Only in the B1 and in the B5 models $10^{20}$eV protons are not too much deflected after 30 Mpc of propagation, and their deflection also peaks at small angles after 100 Mpc.

This is consistent with previous results that investigated the propagation of UHECRs (also taking into account their energy losses) with *ENZO* simulation and a similarly large primordial field (Hackstein et al. 2016, 2019).

In summary, we find that among the investigated models there is the theoretical possibility of detecting signatures of the topology of seed magnetic fields in voids, through the clustering of $10^{20}$eV events from very nearby $\leqslant 10$ Mpc sources. Unluckily, the statistics of such events is presently so small, that such analysis will be dominated by sample variance in the real case (Hackstein et al. 2019).

## 4 DISCUSSION

### 4.1 Numerical & physical limitations

A few important limitations to our work, connected to the employed numerical scheme, must be taken into account in the interpretation of our results.

Probably, the most important limitation of this set of simulation is the adopted spatial resolution, which combined with our subgrid dynamo model is enough to follow the evolution of magnetic fields and shocks on $\geqslant 200$kpc scales (as discussed in several previous work, e.g. Vazza et al. 2014a,b), but likely not enough to simulate cell-by-cell fluctuations of RM, which are key to interpret the structure functions discussed in Sec. 3.2.2. We present in the Appendix the additional tests with a smaller series of runs, designed to test the dependence of our results on the adopted spatial resolution. As expected, the structure function for RM shows a significant, albeit non-dramatic, evolution with resolution. This presently makes it impossible to firmly establish which of our models for primordial magnetic fields can already be ruled out by comparison with the LOFAR data of O'Sullivan et al. (2020), and only future simulations at a higher resolution will be able to make a quantitative comparison.

We notice that RM fluctuations on scales smaller than the LOFAR synthesised beam (20" i.e . < 150 kpc at z=0.8) would cause wavelength-dependent depolarization (e.g. Burn 1966). In this case, the emission from a population of sources that probe regions of high RM variance on small scales are likely to be missing from the LOFAR data at 144 MHz (i.e. completely depolarized),
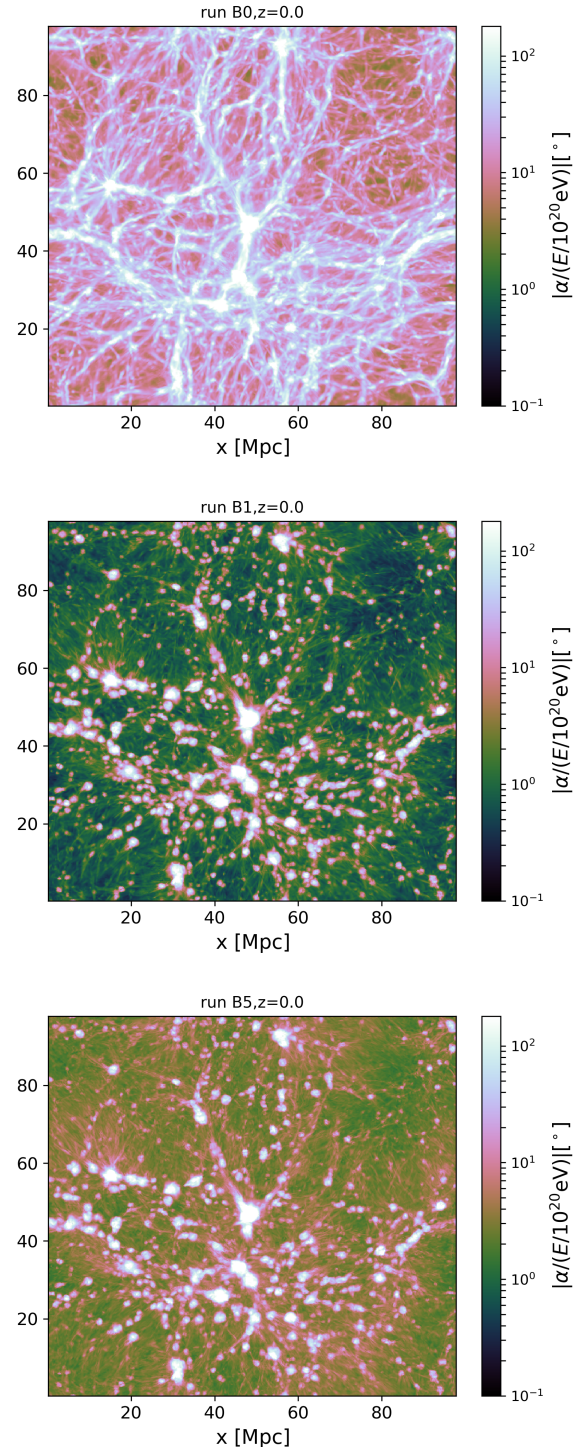


**Figure 17.** Deflection angle for $E = 10^{20}$eV protons, averaged along a 100 Mpc line of sight in models B0, B1 and B5.

but would be present in data at a higher frequency, such as at 1.4 GHz in the NVSS (Vernstrom et al. 2019). Recently, a depolarization study of LOFAR polarized sources found that they have a typical RM dispersion within the beam of $< 0.3$ rad m$^{-2}$ Stuardi et al. (2020). Therefore, any radio galaxy that is embedded in an environment with RM fluctuations larger than this on scales smaller than 20" will not be present in the LOFAR data, but can be de-

**Figure 18.** Trajectories of $E = 10^{19}$eV protons crossing our entire $100^3$Mpc$^3$ volume in models B0, B1 and B5. Each cosmic ray has been randomly injected at the opposite side of the box with respect to the observer.

tected at 1.4 GHz (for RM dispersions up to a few 10s of rad m$^{-2}$). Thus, high resolution simulations, that include radio galaxies embedded in realistic environments that have RM fluctuations on a wide range of scales, can help statistically isolate those sources whose RM variance is dominated by the local environment (e.g. the intracluster medium) and those that are more pristine probes of cosmic filaments.

In this work we were only concerned with ideal MHD, meaning that the resistive dissipation of magnetic fields, the onset of "microscopic" plasma instabilities and other effects related to the departure from a single fluid model were not included (e.g. Schekochihin et al. 2005). We also ran our simulations without explicit viscosity and resistivity, i.e. their magnetic Prandtl number is $P_M = R_M/R_e = \nu/\eta \approx 1$ everywhere by construction. While this assumption is reasonable enough given the existing uncertainties in the properties of space plasmas (e.g. Schekochihin et al. 2004; Brunetti & Lazarian 2011; Beresnyak & Miniati 2016b), it is difficult to assess whether such approximation is valid on all cosmic scales.

Finally, in order to solely focus on the possible differences between variation of primordial seeding models, we neglected alternative scenarios for the seeding of magnetic fields related with galactic activity (e.g. Kulsrud et al. 1997; Kronberg et al. 1999; Völk & Atoyan 2000; Langer et al. 2005; Donnert et al. 2009; Bertone et al. 2006; Samui et al. 2017).

However, the most important differences between primordial models we find concern the very peripheral regions of galaxy clusters, or filaments and cosmic voids, in which the impact of "astrophysical" sources of magnetisation must be sub-dominant (e.g. Vazza et al. 2017; Hackstein et al. 2019). Therefore, the main differences found in this work are very likely to persist regardless of other sources of magnetisation in large-scales, if primordial magnetic fields do exist.

## 5 CONCLUSIONS

We presented cosmological magneto-hydrodynamical simulations for six different initialisations of "primordial" seed magnetic field. We adopted models designed to be compatible with the conservative upper limits of non-helical primordial magnetic fields derived from the latest Planck, BICEP/Keck Array, SPT CMB anisotropy power spectra data as constrained in Paoletti & Finelli (2019). We investigated the impact of the scale dependence of primordial magnetic fields by assuming a stochastic background, spanning differ-

ent possible field configurations. The scale dependence is related to the generation mechanism and advance in this topic could be important in the understanding of the physics of the early Universe. In particular, causal mechanisms, mainly related to first-order phase transitions and second-order perturbations, require a spectral index $\alpha \geqslant 2.0$ that represents the extreme blue limit of our analysis. Inflationary mechanism can instead generate fields with also "red" spectra, that we sample starting from the lowest infrared limit $\alpha = -2.9$. We have limited our analysis to the effect of primordial magnetic fields at the stochastic background level, leaving the study of a modified matter power spectrum due to magnetised cosmological perturbations for a future work.

We find that while matter halos at low-$z$ do not retain memory of seed fields (due to the fact that their magnetic field is dominated by dynamo amplification), their outskirts, filaments and voids might retain traces of the topology and amplitude of the primordial fields.

Our main findings can be so summarised as follows:

• different models of primordial seed fields, all designed to be consistent with the most recent conservative constraints from the combination of the recent CMB data of Planck 2018 and ground based observatory BICEP/KECK and South Pole Telescope (Paoletti & Finelli 2019), produce significant differences in the average strength and topology of magnetic fields in the less dense cosmic environment, i.e. for $\rho \leqslant 10^{-30}$ g/cm$^3$, even down to $z = 0$;

• depending on the amplitude of magnetic field fluctuations at small scales ($\ll 10$ Mpc) additional gas perturbances, eventually leading to shock waves, are driven in the most rarefied cosmic gas, additionally to "standard" structure formation shocks (albeit adding little extra energy in the total volume);

• all variations of the magnetic field scenarios have no relevant impact on the formation of structures, at least for the $\geqslant 10^{12}$M$_\odot$ masses probed in this work;

• the investigated properties of magnetic fields in galaxy clusters, and of the observables connected to them, are almost invariant within $\leqslant$ R$_{200}$ of simulated clusters. Differences between models, which can be ideally detected under perfect observing conditions, are instead present in the most peripheral regions of clusters, $\geqslant$ R$_{200}$, which are at the edge of detectability with present (or future) instruments.

• The Faraday Rotation Measure and the radio synchrotron emission produced in the different are significantly different in the outskirts of galaxy clusters, in cosmic filaments and in voids. Differences between models can be preferentially detected in a statisti-
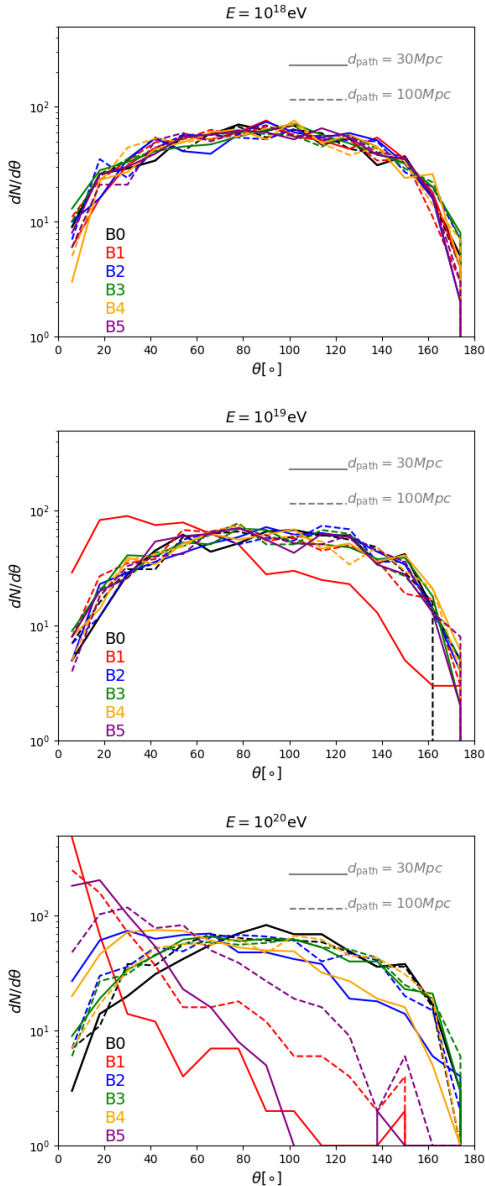
**Figure 19.** Distribution of deflection angles for simulated UHECR protons with an initial energy $E = 10^{18}$eV (top) or $E = 10^{19}$eV (centre) and $E = 10^{20}$eV (bottom), injected with initial random positions and velocities in our simulated volumes. The different linestyles in both panels show the distribution of deflection angles after propagating for 30 Mpc (solid) or 100 Mpc (dashed).

cal way on large cosmic volumes (in this work we tested lightcones reaching out to $z = 0.8$).

• We preliminary compared with recent available tests of the cross-correlation between galaxies and diffuse synchrotron emission using MWAW (Vernstrom et al. 2017) or of the RM structure function from physical pairs of radio sources (O'Sullivan et al. 2020). These tests suggest that existing surveys may already be employed to constrain primordial models of magnetism as some of the investigated models already produce too strong signals to be compatible with observations. The limited resolution available in these runs prevent us however from firm conclusions about which models are allowed by present radio observations.

• significant differences are in principle detectable in the average deflection angle experienced by UHECRs ($10^{20}$ eV) as they probe large scales of the seed magnetic field distributions in voids, which persists until $z = 0$.

To summarise, in this work we have established for the first time a direct link between primordial magnetic fields (as constrained by the CMB anisotropy power spectra) and the nowadays cosmic magnetism (as it can be directly observed with radio observatories and through the propagation of charged cosmic rays). As initial conditions, we considered the most conservative Planck 2018 - BICEP/KECK - SPT constraints on primordial magnetic fields, resulting from their gravitational effects on CMB anisotropies: the allowed comoving amplitude of the stochastic background ranges from few nano-Gauss to few pico-Gauss, depending on its scale dependence (note that tighter limits might be even obtained by considering additional effects, such as post-recombination heating, or CMB higher order statistics). The variation of the amplitude with the configuration is the key point in understanding the results: blue power spectra which increase the power on the smallest scales are already strongly constrained to very low amplitude by the CMB, whereas fields with more infrared spectra are allowed to larger amplitudes, yet with diluted power on much larger scales. The interplay between the scale dependence of the fields, and the constraints on their amplitude by the CMB, is perfectly reflected in our simulation results.

This research program is expected to advance on different fronts, also following the deployment of new instruments. For example future CMB experiments as LiteBIRD (Hazumi et al. 2019) [6] and ground based observatories as Simons Observatory (Ade et al. 2019)[7] will further tighten the constraints on the amplitude of the fields especially on very blue spectra with Simons observatory and infrared spectra with LiteBIRD reaching the subnanoGauss and subopicoGauss level (Paoletti & Finelli 2019).

On the theoretical side, progresses on the impact on the ionization history (Kunze & Komatsu 2015; Chluba et al. 2015; Paoletti et al. 2019) could allow to further tighten the CMB constraints used here, which could be also made more accurate by including the modification to the matter power spectrum induced by primordial magnetic fields.

Jointly with the effort of increasing the resolution of the simulations, these advances can further bridge the connection between early and late cosmic magnetism to understand its origins.

[6]  A joint satellite mission JAXA-US-Europe to study the large scale polarization of the CMB with unprecedented sensitivity with launch in 2027.
[7]  Ground based observatory that will observe the 40% of the sky on the smallest scales with high sensitivity, will start acquiring data in 2021.

## DATA AVAILABILITY

The code used to produce the simulations discussed in this paper is public (enzo-project.org). The method to produce initial conditions necessary to perform the simulations are documented in the paper, and the 3-dimensional files can be shared by the authors upon request.

## REFERENCES

Adamek J., Durrer R., Fenu E., Vonlanthen M., 2011, JCAP, 1106, 017

Ade P., et al., 2018, in 53rd Rencontres de Moriond on Cosmology

Ade P., et al., 2019, JCAP, 02, 056

Ahonen J., Enqvist K., 1998, Phys. Rev., D57, 664

Akrami Y., et al., 2018

Alves Batista R. et al., 2016, Journal of Cosmology and Astroparticle Physics, 5, 038

Alves Batista R., Sigl G., 2014, Journal of Cosmology and Astroparticle Physics, 11, 031

Arlen T. C., Vassilev V. V., Weisgarber T., Wakely S. P., Yusef Shafi S., 2014, ApJ, 796, 18

Ashoorioon A., Mann R. B., 2005, Phys. Rev., D71, 103509

Ballardini M., Finelli F., Paoletti D., 2015, JCAP, 1510, 031

Bamba K., Yokoyama J., 2004, Phys. Rev., D69, 043507

Banfi S., Vazza F., Wittor D., 2020, arXiv e-prints, arXiv:2006.10063

Barrow J. D., Ferreira P. G., Silk J., 1997, Physical Review Letters, 78, 3610

Baym G., Bodeker D., McLerran L. D., 1996, Phys. Rev., D53, 662

Beck A. M., Lesch H., Dolag K., Kotarba H., Geng A., Stasyszyn F. A., 2012, MNRAS, 422, 2152

Beresnyak A., Miniati F., 2016a, ApJ, 817, 127

Beresnyak A., Miniati F., 2016b, ApJ, 817, 127

Berezinsky V., 2014, Astroparticle Physics, 53, 120

Bertone S., Vogt C., Enßlin T., 2006, MNRAS, 370, 319

Biermann P. L. et al., 2016, ArXiv e-prints

Boyanovsky D., de Vega H. J., 2005, AIP Conf. Proc., 784, 434

Brandenburg A., Kahniashvili T., 2017, Phys. Rev. Lett., 118, 055102

Broderick A. E., Chang P., Pfrommer C., 2012, ApJ, 752, 22

Brüggen M., Ruszkowski M., Simionescu A., Hoeft M., Dalla Vecchia C., 2005, ApJL, 631, L21

Brunetti G., Jones T. W., 2014, International Journal of Modern Physics D, 23, 1430007

Brunetti G., Lazarian A., 2011, MNRAS, 410, 127

Bryan G. L. et al., 2014, ApJS, 211, 19

Burn B. J., 1966, MNRAS, 133, 67

Bykov A. M., Vazza F., Kropotina J. A., Levenfish K. P., Paerels F. B. S., 2019, Science & Space Review, 215, 14

Caldwell R. R., Motta L., Kamionkowski M., 2011, Phys. Rev., D84, 123525

Campanelli L., 2009, International Journal of Modern Physics D, 18, 1395

Caprini C., Durrer R., Kahniashvili T., 2004, Phys. Rev., D69, 063006

Caprini C., Durrer R., Servant G., 2009, JCAP, 0912, 024

Caprini C., Gabici S., 2015, Physical Review Letters, 91, 123514

Caprioli D., Spitkovsky A., 2014, ApJ, 783, 91

Chen W., Buckley J. H., Ferrer F., 2015, Physical Review Letters, 115, 211103

Chernin A. D., 1967, Sovietic Astronomy, 10, 634

Chluba J., Paoletti D., Finelli F., Rubiño-Martín J.-A., 2015, Mon. Not. Roy. Astron. Soc., 451, 2244

Cho J., 2014, ApJ, 797, 133

Christensson M., Hindmarsh M., Brandenburg A., 2001, Phys. Rev., E64, 056405

Christensson M., Hindmarsh M., Brandenburg A., 2005, Astron. Nachr., 326, 393

Csáki C., Kaloper N., Peloso M., Terning J., 2003, Journal of Cosmology and Astroparticle Physics, 5, 005

Dedner A., Kemm F., Kröner D., Munz C.-D., Schnitzer T., Wesenberg M., 2002, Journal of Computational Physics, 175, 645

Demozzi V., Mukhanov V., Rubinstein H., 2009, JCAP, 0908, 025

Dolag K., Bartelmann M., Lesch H., 1999, A & A, 348, 351

Dolag K., Evrard A., Bartelmann M., 2001, A & A, 369, 36

Dolag K., Grasso D., Springel V., Tkachev I., 2005, Journal of Cosmology and Astroparticle Physics, 1, 9

Dolag K., Kachelrieß M., Ostapchenko S., Tomàs R., 2009, ApJ, 703, 1078

Dolag K., Kachelriess M., Ostapchenko S., Tomàs R., 2011, ApJL, 727, L4

Donnert J., Dolag K., Lesch H., Müller E., 2009, MNRAS, 392, 1008

Donnert J., Vazza F., Brüggen M., ZuHone J., 2018, ArXiv e-prints

Durrer R., Caprini C., 2003, JCAP, 0311, 010

Ellis J., Fairbairn M., Lewicki M., Vaskonen V., Wickens A., 2019, JCAP, 1909, 019

Fedeli C., Moscardini L., 2012, JCAP, 11, 055

Federrath C., Schober J., Bovino S., Schleicher D. R. G., 2014, ApJL, 797, L19

Fenu E., Pitrou C., Maartens R., 2011, Mon. Not. Roy. Astron. Soc., 414, 2354

Fidler C., Pettinari G., Pitrou C., 2016, Phys. Rev., D93, 103536

Field G. B., Carroll S. M., 2000, Phys. Rev., D62, 103008

Finelli F., Paci F., Paoletti D., 2008, Phys. Rev., D78, 023510

Fujita T., Namba R., Tada Y., Takeda N., Tashiro H., 2015, JCAP, 1505, 054

Gheller C., Pantano O., Moscardini L., 1998, MNRAS, 296, 85

Gheller C., Vazza F., 2019, MNRAS, 486, 981

Gheller C., Vazza F., 2020, MNRAS, 494, 5603

Giovannini M., Shaposhnikov M. E., 2000, Phys. Rev., D62, 103512

Grasso D., Riotto A., 1998, Phys. Lett., B418, 258

Grete P., Vlaykov D. G., Schmidt W., Schleicher D. R. G., 2016, Physics of Plasmas, 23, 062317

Guo X., Sironi L., Narayan R., 2014, ApJ, 794, 153

Haardt F., Madau P., 1996, ApJ, 461, 20

Hackstein S., Brüggen M., Vazza F., Gaensler B. M., Heesen V., 2019, MNRAS, 488, 4220

Hackstein S., Vazza F., Brüggen M., Sigl G., Dundovic A., 2016, MNRAS, 462, 3660

Hackstein S., Vazza F., Brüggen M., Sorce J. G., Gottlöber S., 2017, ArXiv e-prints

Hazumi M., et al., 2019, J. Low Temp. Phys., 194, 443

Hindmarsh M., Everett A., 1998, Phys. Rev., D58, 103505

Hoeft M., Brüggen M., 2007, MNRAS, 375, 77

Horns D., Maccione L., Meyer M., Mirizzi A., Montanino D., Roncadelli M., 2012, Physical Review Letters, 86, 075024

Hutschenreuter S., Dorn S., Jasche J., Vazza F., Paoletti D., Lavaux G., Enßlin T. A., 2018, Classical and Quantum Gravity, 35, 154001

Jain R. K., Durrer R., Hollenstein L., 2014, J. Phys. Conf. Ser., 484, 012062

Jedamzik K., Saveliev A., 2019, Physical Review Letters, 123, 021301

Jones T. W., Porter D. H., Ryu D., Cho J., 2011, Memorie della Societá Astronomica Italiana, 82, 588

Kahniashvili T., Brandenburg A., Durrer R., Tevzadze A. G., Yin W., 2017, JCAP, 1712, 002

Kahniashvili T., Brandenburg A., Tevzadze A. G., 2016, Physica Scripta, 91, 104008

Kahniashvili T., Maravin Y., Lavrelashvili G., Kosowsky A., 2014, Phys. Rev., D90, 083004

Kahniashvili T., Maravin Y., Natarajan A., Battaglia N., Tevzadze A. G., 2013, ApJ, 770, 47

Kanno S., Soda J., Watanabe M.-a., 2009, JCAP, 0912, 009

Keisler R., et al., 2015, Astrophys. J., 807, 151

Kronberg P. P., Lesch H., Hopp U., 1999, ApJ, 511, 56

Kulsrud R. M., Cen R., Ostriker J. P., Ryu D., 1997, ApJ, 480, 481

Kunze K. E., 2012, Phys. Rev. D, 85, 083004

Kunze K. E., Komatsu E., 2015, JCAP, 1506, 027

Langer M., Aghanim N., Puget J.-L., 2005, A & A, 443, 367

Mack A., Kahniashvili T., Kosowsky A., 2002, Phys. Rev., D65, 123004

Marinacci F., Vogelsberger M., Mocz P., Pakmor R., 2015, MNRAS, 453, 3999

Matarrese S., Mollerach S., Notari A., Riotto A., 2005, Phys. Rev., D71, 043502

Meyer M., Conrad J., Dickinson H., 2016, ApJ, 827, 147

Montanino D., Vazza F., Mirizzi A., Viel M., 2017, Physical Review Letters, 119, 101101

Neronov A., Vovk I., 2010, Science, 328, 73

O'Sullivan S. P. et al., 2020, MNRAS, 495, 2607

Pakmor R., Marinacci F., Springel V., 2014, ApJL, 783, L20

Paoletti D., Chluba J., Finelli F., Rubino-Martin J. A., 2019, Mon. Not. Roy. Astron. Soc., 484, 185

Paoletti D., Finelli F., 2011, Phys. Rev., D83, 123533

Paoletti D., Finelli F., 2013, Phys. Lett., B726, 45

Paoletti D., Finelli F., 2019

Planck Collaboration et al., 2016, A & A, 594, A19

Pogosian L., Vachaspati T., Winitzki S., 2003, New Astron. Rev., 47, 859, [,132(2002)]

Porter D. H., Jones T. W., Ryu D., 2015, ApJ, 810, 93

Quashnock J. M., Loeb A., Spergel D. N., 1989, Astrophys. J., 344, L49

Raffelt G., Stodolsky L., 1988, Physical Review Letters, 37, 1237

Ratra B., 1992, Astrophys. J., 391, L1

Rieder M., Teyssier R., 2016, MNRAS, 457, 1722

Rieder M., Teyssier R., 2017, ArXiv e-prints

Ryu D., Das S., Kang H., 2010, ApJ, 710, 1422

Ryu D., Kang H., Cho J., Das S., 2008, Science, 320, 909

Ryu D., Schleicher D. R. G., Treumann R. A., Tsagas C. G., Widrow L. M., 2012, Science & Space Review, 166, 1

Samui S., Subramanian K., Srianand R., 2017, ArXiv e-prints

Sanati M., Revaz Y., Schober J., Kunze K. E., Jablonka P., 2020, arXiv e-prints, arXiv:2005.05401

Saveliev A., Jedamzik K., Sigl G., 2013, Phys. Rev., D87, 123001

Schekochihin A. A., Cowley S. C., Kulsrud R. M., Hammett G. W., Sharma P., 2005, ApJ, 629, 139

Schekochihin A. A., Cowley S. C., Taylor S. F., Maron J. L., McWilliams J. C., 2004, ApJ, 612, 276

Semikoz V. B., Sokoloff D., 2005, A & A, 433, L53

Sethi S. K., Subramanian K., 2005, Mon. Not. Roy. Astron. Soc., 356, 778

Sharma R., Subramanian K., Seshadri T. R., 2018, Phys. Rev., D97, 083503

Shaw J., Lewis A., 2010, Phys. Rev. D, 81, 043517

Shaw J. R., Lewis A., 2012, Phys. Rev., D86, 043510

Shu C.-W., Osher S., 1988, Journal of Computational Physics, 77, 439

Sigl G., 2002, Phys. Rev., D66, 123002

Sigl G., Miniati F., Ensslin T. A., 2003, Phys. Rev., D68, 043002

Sigl G., Olinto A. V., Jedamzik K., 1997, Phys. Rev., D55, 4582

Sol H. et al., 2013, in IAU Symposium, Vol. 294, Solar and Astrophysical Dynamos and Magnetic Activity, Kosovichev A. G., de Gouveia Dal Pino E., Yan Y., eds., pp. 459–470

Soler J. D., Hennebelle P., 2017, A & A, 607, A2

Stuardi C. et al., 2020, A & A, 638, A48

Tavecchio F., Roncadelli M., Galanti G., Bonnoli G., 2012, Physical Review Letters, 86, 085036

Tevzadze A. G., Kisslinger L., Brandenburg A., Kahniashvili T., 2012, Astrophys. J., 759, 54

Trivedi P., Reppin J., Chluba J., Banerjee R., 2018, MNRAS, 481, 3401

Turner M. S., Widrow L. M., 1988, Physical Review Letters, 37, 2743

Törnkvist O., Davis A.-C., Dimopoulos K., Prokopec T., 2001, AIP Conf. Proc., 555, 443

Völk H. J., Atoyan A. M., 2000, ApJ, 541, 88

Vachaspati T., 1991, Phys. Lett., B265, 258

Vachaspati T., 2001, Phys. Rev. Lett., 87, 251302

van Weeren R. J., de Gasperin F., Akamatsu H., Brüggen M., Feretti L., Kang H., Stroe A., Zandanel F., 2019, Science & Space Review, 215, 16

Vazza F., Brueggen M., Gheller C., Hackstein S., Wittor D., Hinz P. M., 2017, Classical and Quantum Gravity

Vazza F., Brüggen M., Gheller C., Wang P., 2014a, MNRAS, 445, 3706

Vazza F., Brunetti G., Brüggen M., Bonafede A., 2018, MNRAS, 474, 1672

Vazza F., Brunetti G., Gheller C., 2009, MNRAS, 395, 1333

Vazza F., Dolag K., Ryu D., Brunetti G., Gheller C., Kang H., Pfrommer C., 2011, MNRAS, 418, 960

Vazza F., Ferrari C., Brüggen M., Bonafede A., Gheller C., Wang P., 2015, A & A, 580, A119

Vazza F., Gheller C., Brüggen M., 2014b, ArXiv e-prints

Vazza F., Jones T. W., Brüggen M., Brunetti G., Gheller C., Porter D., Ryu D., 2017, MNRAS, 464, 210

Vernstrom T., Gaensler B. M., Brown S., Lenc E., Norris R. P., 2017, MNRAS, 467, 4914

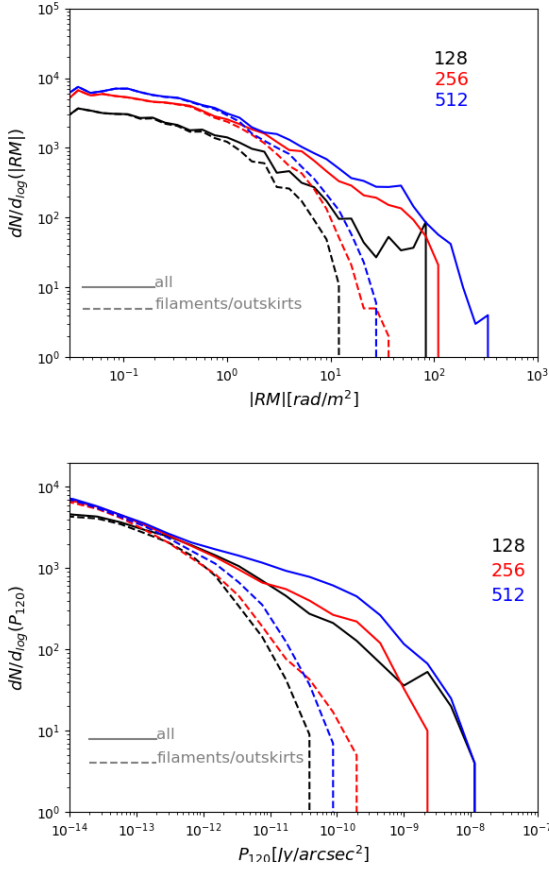Vernstrom T., Gaensler B. M., Rudnick L., Andernach H., 2019,

**Figure A1.** Distribution functions of Faraday Rotation (top) and of synchrotron radio emission at 1.4 GHz (bottom) in our resolution tests, for a $1\circ \times 1°$ field of view integrated for a light cone up to $z = 0.8$.

**Figure A2.** Simulated distribution of $(\Delta RM(\Delta\theta)^2)$ as a function of angular separation for our three resolution tests for a small $25^3$Mpc$^3$ box.

ApJ, 878, 92

Widrow L. M., 2002, Reviews of Modern Physics, 74, 775

Widrow L. M., Ryu D., Schleicher D. R. G., Subramanian K., Tsagas C. G., Treumann R. A., 2012, Science & Space Review, 166, 37

Wittor D., Jones T., Vazza F., Brüggen M., 2017a, MNRAS, 471, 3212

Wittor D., Vazza F., Brüggen M., 2017b, MNRAS, 464, 4448

Wittor D., Vazza F., Ryu D., Kang H., 2020, MNRAS, 495, L112

Xu H., Li H., Collins D. C., Li S., Norman M. L., 2009, ApJL, 698, L14

Zel'dovich Y. B., 1970, Sovietic Astronomy, 13, 608

Zhang Y., Vachaspati T., Ferrer F., 2019, Phys. Rev., D100, 083006

Zucca A., Li Y., Pogosian L., 2017, Phys. Rev., D95, 063506

# APPENDIX A: RESOLUTION TESTS

To test for the dependence on the spatial/mass resolution of our results, we resimulated a smaller $25^3$ Mpc$^3$ volume with the same set of cosmological parameters of the main paper, using from $128^3$, $256^3$ and $512^3$ cells, which gives a comoving spatial resolution of 195 kpc (as in our main paper), 97.6 kpc and 48.8 kpc, respectively. We limited to 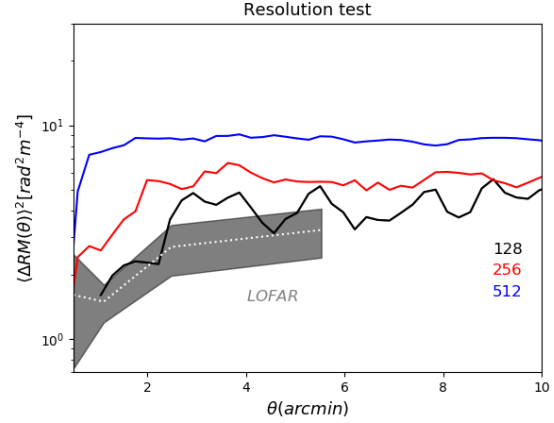the simple uniform seed magnetic field model with $B_0 = 2$ nG, and applied the same sub-grid model for small-scale dynamo amplification as in the main paper. Using the same approach of the main paper, we produced mock light-cones of radio observables up to $z = 0.8$, with the limitation that the very limited volume of this box does introduce artefacts in the final light cone, as the same structures are bound to repeat several time to fill the simulated $1° \times 1°$ field of view. Fig. A1 shows the distribution of integrated Faraday Rotation and synchrotron emission for the light cones in the three runs. The distributions have a remarkably similar shape across resolutions, especially in the range of filaments and cluster outskirts, which is the most interesting for our study.

However, the increase of small-scale features in the gas flow internal to filaments does produce an evolution with resolution in the mock distribution of RM structure function, as shown in Fig. A2. While the 128 case looks in the range of what found in the main paper at the same resolution (albeit with a large scatter due to the small statistics of this box), the other two runs produced a higher level of $)\langle \Delta RM(\theta)\rangle)^2$ at most scales. Incidentally, the 256 run has a resolution close to the simulation used in our recent comparison with LOFAR data O'Sullivan et al. (2020), and once rescaled for the same initial magnetic field amplitude give a similar trend. Although not dramatic, considering the $\times 4$ increase in spatial resolution and the $\sim 4^3$ increased mass resolution, these resolution trends suggest that the absolute level of the RM structure function obtained in our main paper must be taken with care, due to the emergence of small-scale structures affects this observable more than others.

Fig. A3 gives the projected magnetic field strength across the simulated box, and the projected synchrotron radio emission from shocks, computed as in the main paper. The large scale distribution of magnetic fields is remarkably similar on all scales, which also confirms that the our sub-grid dynamo model is well behaved across resolutions, despite the progressive increase of the Reynolds number of the gas flow within galaxy clusters. On the other hand, as expected shocks are increasingly better resolved in cluster outskirts, and finer details in the morphology of synchrotron emission internal to large-scale structures appear.

As a caveat, we shall notice that although these tests concerned the evolution of magnetic field topology/amplitude within filaments and cosmic structures, they cannot test the physical effects of sampling a higher $k_D$ (i.e. a smaller cutoff scale) in simulated primordial fields.
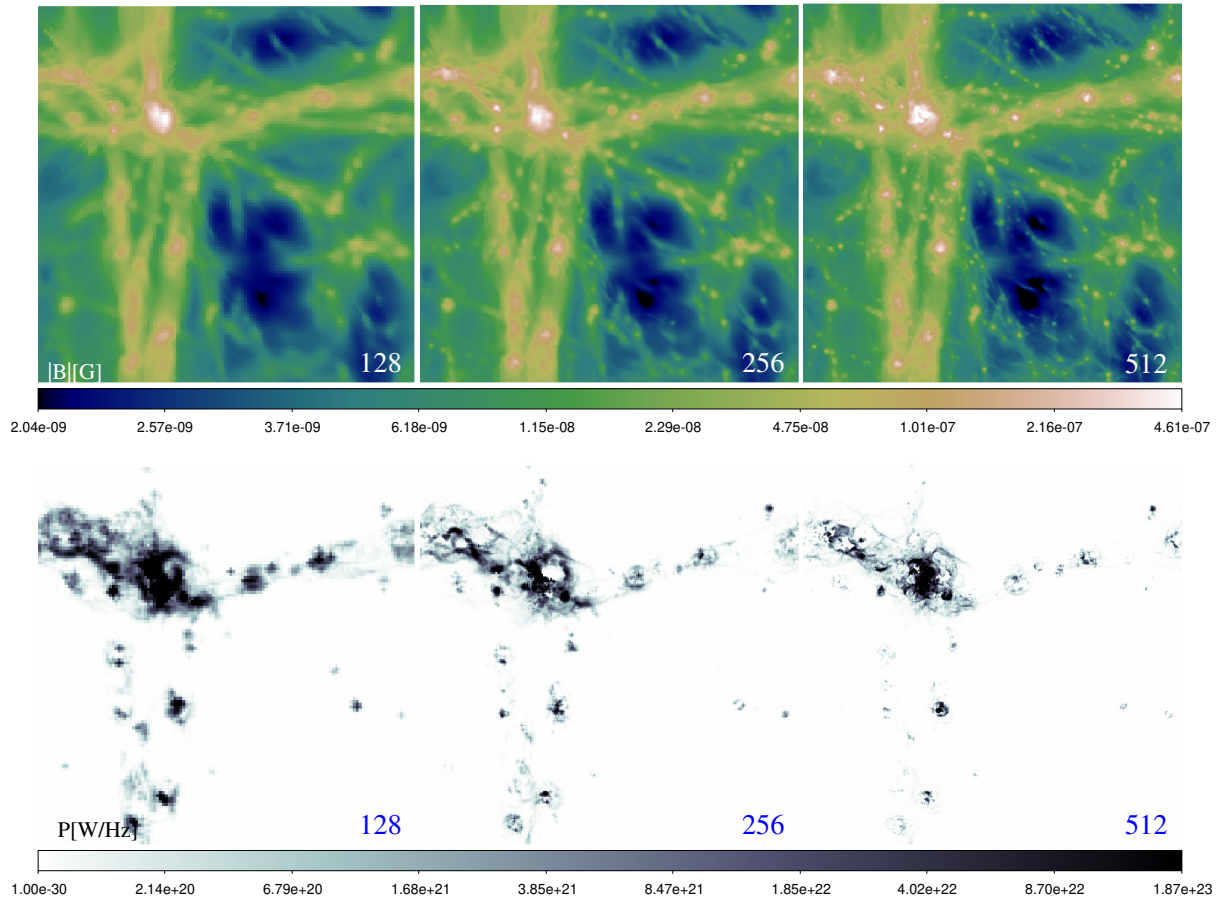
**Figure A3.** Maps of projected magnetic field strength (top) and synchrotron radio power (bottom) for our resolution tests at $z = 0$.